Viral transport in evaporating sessile model respiratory droplets

Javier Martínez-Puig[a], Carlos de la Torre Luque[a], Carolina Arbesu Nieto[a], Pepijn Hoekstra[c], Fernando Usera[b], Beatriz Martín Jouve[b], Aránzazu de la Encina[b], Teresa Bartolomé[b], Marta Sanz[b], Fernando Almazán[b], Ana Oña[b], Alvaro Marin[c], and Javier Rodríguez-Rodríguez[a,1]

[a]Carlos III University of Madrid, Department of Thermal and Fluids Engineering, Leganés, 28911, Spain
[b]Centro Nacional de Biotecnología, Consejo Superior de Investigaciones Científicas CSIC, Madrid, Spain
[c]Department of Physics of Fluids, University of Twente, Enschede, The Netherlands
[1]To whom correspondence should be addressed. E-mail: bubbles@ing.uc3m.es

September 30, 2025

Abstract

Viral particles, or virions, remain infectious in the dry residue of respiratory droplets for times as long as hours [1, 2, 3]. This is surprising, since salt concentration increases dramatically as the drop's water evaporates, making the drop a harsh environment for virions [4]. A plausible hypothesis to explain the slow decay of viral infectivity is that the main solution components (mainly virions, salt and protein [5]) segregate during the evaporation, with virions being transported away from salt deposits, protecting them from the salt's damaging effects [1]. Understanding where virions reside in a drop residue is essential to disentangle the physico-chemical mechanisms that drive their inactivation [6]. However, determining the virion location in an environment as heterogeneous and complex as a sessile drop is experimentally challenging. Here we use electron microscopy in the drop's dry remains to show that virions are found mainly forming aggregates in protein-rich regions of the residue, away from salt crystals. Previous works have also attempted to detect the presence of virions in drop residues, with inconclusive results due to experimental limitations [5, 7, 8]. Additionally, neither the physical mechanism behind the observed viral distributions were properly described in previous works. In this work, we complement our experimental observations with a theoretical description of the flow inside the drop, which allows to elucidate the transport mechanisms yielding the observed viral spatial distribution. The theoretical transport model, supported by experiments, allows us to rationalize the spatial distribution of salt, protein, and virions inside evaporating respiratory drops. We anticipate our results to be an essential ingredient to explain the discrepancies between the infectivity decay rates measured in respiratory drops, which nowadays exhibit important discrepancies [9].

Viruses and other pathogens are able to remain infective in the dry residue of a respiratory drop for hours or even days [1]. A priori, this is rather counterintuitive since, as the drop loses its water content to evaporation, the salt concentration inside the drop increases to levels high enough to inactivate any virion present in the drop in a much shorter time scale [1, 4, 10]. Two explanations for this apparent paradox have been proposed in the literature. First, that the presence of organic compounds in respiratory fluids, most notably the glycoprotein mucin, protects virions from the damaging effect of salt ions [11, 12]. Second, that once the water content of the drop is lost to evaporation, salt precipitates into crystals, which self-segregate spatially from virions [1]. This second hypothesis is consistent with the observation that the decay rate of Influenza is higher during the evaporation process than after the residue has dried [13, 10]. However, these findings are contradicted by other authors. For instance, Rockey and coworkers [14] observed that, in some circumstances, an elevated salt (i.e., ion) concentration was linked to a slower inactivation rate for Influenza virus.

This example illustrates the discrepancies found across different studies in the literature [9]. We can conclude that, despite the significant progress on the matter, the precise physico-chemical mechanisms that drive viral inactivation inside respiratory drops are still unknown [15]. A critical missing ingredient to unravel these mechanisms is to know where virions are located inside the dry residue of the droplets as water evaporates [5, 6, 12], and equally important, what is the physico-chemical microenvironment that surrounds them there. Direct observation of the virions inside the drop residue would partly settle this question, but this is not a trivial task. Although there exist many techniques to visualize virions in purified suspensions [16, 17] or in homogeneous, diluted gel-like structures [11, 18, 17], visualizing the distribution of a large number of viral particles in complex heterogeneous structures, like the residue of a respiratory drop [19], is still challenging.

One of the first attempts to visualize the viral distribution within a drop was made by Vejerano & Marr [5]. They used a non-specific fluorescent tagging on the $\phi 6$ phage to localize these virions in the residue of a drop of artificial saliva. They found isolated fluorescent spots compatible with virions distributed without any specific spatial pattern in the dry residue of the drop. Unfortunately, the limited number of experiments reported and the fact that the fluorescent dye may bind to other molecules present in the drop preclude the authors from drawing quantitative conclusions about the distribution of virions in the residue. More recently, Kong and coworkers [8] used fluorescence microscopy with GFP-labeled particles of vesicular stomatitis virus to show that these virions form agglomerates, chiefly settling around the innermost part of the rim of dry sessile droplets. In their work, however, the authors do not describe the mechanisms that transport the virions to that location. More importantly, their experimental technique does not allow them to determine the structure of the microenvironment where virions lie, a crucial matter to understand the mechanisms that lead to their slow inactivation. Furthermore, their fluorescence-based technique is only sensitive to agglomerates of fluorescence-labeled virions and therefore unable to detect the presence of virions in other regions where still their concentration may be substantial. More recently, Pan and coworkers from Lindsey Marr's lab [12] studied the distribution of labeled Influenza A virions in the dry residue of both model respiratory (a mixture of PBS and Mucin) and human saliva droplets evaporating at low, medium, and high relative humidity. For drops with physiological protein concentration and for saliva they observed that virions predominantly concentrate close to the drop's rim at low (20%) and medium (50%) humidity. For high (80%) humidity virions spread more uniformly and even concentrate close to the center. These distributions mainly coincide with those of the protein itself.

Although the above mentioned studies shed light on the distribution of virions in the residue of the drop, they do not explain in a quantitative manner the processes that lead to the observed viral and protein distribution. In other words, to the formation of the microenvironment that dictates how virions degrade. Indeed, we believe that understanding the transport of virions, proteins, and salt in the evaporating respiratory drop is essential to develop quantitative viral inactivation models based on first principles. We highlight that the influence of the environmental conditions on which the drop evaporates affects the viral infectivity through their effect on the drop hydrodynamics [4, 15, 12]. With this motivation, in this work we study experimentally and theoretically the transport of virions, protein, and salt in model respiratory droplets.

In contrast to other studies, we use Transmission Electron Microscopy (TEM) to examine the dry residue of model respiratory droplets. To achieve this, we lower the concentrations of non-volatile components in the droplet to a point where we can still observe virions without altering significantly the evaporation-driven flow that develops within during the drying process. As experimental viral model, we use the porcine coronavirus transmissible gastroenteritis virus (TGEV) that belongs to the genus alphacoronavirus of the Coronaviridae family within the Nidovirales order [20]. Like other coronaviruses, TGEV is an enveloped, spherical virus with a single-stranded positive-sense RNA genome and a diameter of approximately 110 nm [21]. Structurally, TGEV closely resembles human coronaviruses of significant public health concern, such as SARS-CoV-2, making it an excellent surrogate for studying coronavirus dynamics and stability in respiratory droplets [17]. Notably, TGEV can be propagated to high titres, it is easy to purify, and can be handled in a BSL-2 laboratory, which simplifies experimental procedures. Thanks to high titres TGEV can reach, we are able to observe a

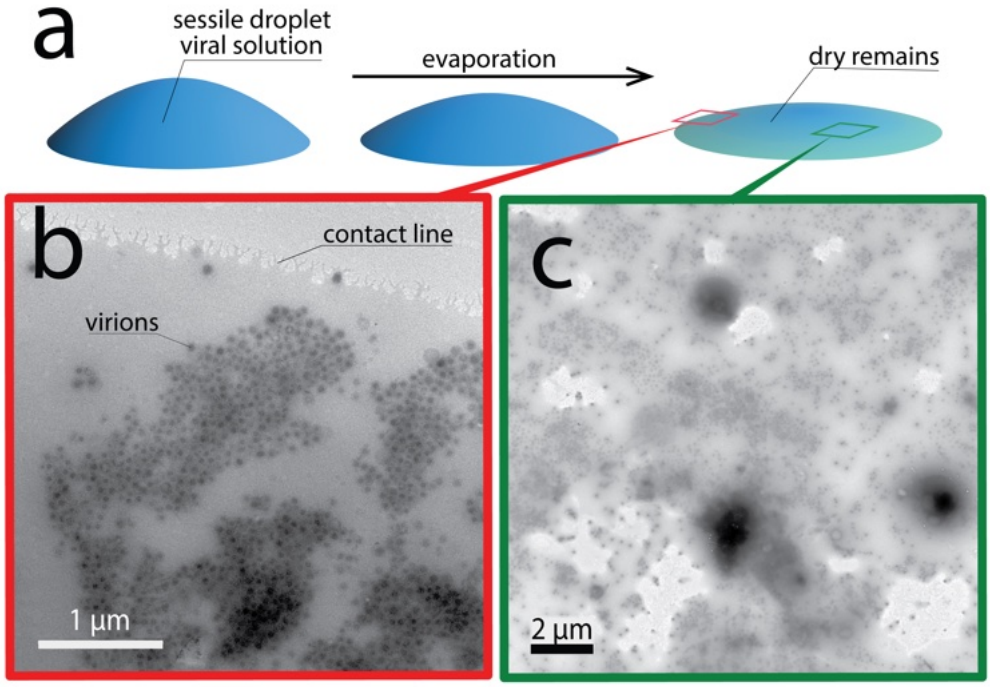

Figure 1: (a) Sketch of the process: sessile droplets containing a viral solution of the coronavirus TGEV, mucin proteins and salts are evaporated on top of a TEM grid until only a dry residue is left. Panels (b) and (c) show TEM images of the dry residue for such model respiratory sessile droplets evaporated at RH 40 %. (b) Corresponds to an image of the rim region (region highlighted in red in sketch (a)). Panel (c) is a close-up of a region close to the drop center (green square in (a)).

large number of virion-laden structures with a reasonably small number of experiments and hence to draw conclusions about the virion distribution. Additionally, we also carry out a theoretical study, validated with dedicated experiments without virions, to elucidate the physical mechanisms that shape the structure and distribution of virions and other solutes in the dry drop residue.

Virion distribution in the drop residue

Experiments on evaporating model respiratory droplets containing TGEV were performed at two relative humidity values: RH = 40 % and RH = 70 %. In what follows, we will refer to these two conditions simply as *low* and *high humidity*. Then, the dry residues of the model respiratory droplets were examined using TEM (See Methods).

At first glance, our TEM images support the findings of previous studies that employed fluorescence microscopy to investigate the overall distribution of virions [8, 12]. Using humidity values between 20% and 50%, these studies reported a significant accumulation of virions in the rim region of the droplet, an observation consistent with our own TEM results (Fig. 1B and 15B). In contrast with standard fluorescence microscopy, TEM allows us to see individual virions and to discover notable features regarding their distribution. One of the most important and unique features that TEM allows us to reveal, is that the virions found in the rim are connected forming large but shallow networks, mostly consisting in monolayers (Fig. 1B). This surprising feature is consistently observed under our TEM conditions, as the depth of field used to acquire the micrographs greatly exceeds the size of a single virion, ensuring that no additional virion layers are present in the images, as those shown in 1b and c.

One would intuitively expect that viral mono- or oligolayers would form more likely with few virions in suspension. Our observations are specially surprising given the high viral titre that we reach with TGEV (see Materials and Methods). The shallow nature of the network suggests that they may have formed at the drop-air interface, in a mechanism similar to that proposed by Bruning

and coworkers [22] for the accumulation of colloidal particles at the liquid-air interface in evaporating salt-solution drops. Given the flatness of the observed virion distribution, this mechanism is the most likely to dominate since it has also been previously observed in similar systems, and there is no physical evidence for other processes. At the lowest evaporation rates, for the residues obtained at high humidity, viral aggregates are still visible but they tend to be smaller (Fig. 16). Also, the distribution of virions is more homogeneous at high humidity, with more virions in the central region of the residue and fewer close to the rim.

Interestingly, either isolated or part of an aggregate, virions are always found in regions rich in protein. This is observed both in dry and humid conditions, and even inside the rim and in the central portion of the residue. This is surprising, since this central portion typically contains low concentration of protein, but nevertheless, it is clear from our images that individual viruses are surrounded by a small protein patch (Fig. 1C and Fig. S14). This observation is in agreement with the conclusion drawn by Wardzala and coworkers [23], who found that mucin binds to the surface of the coronavirus OC43 particles. It also supports the hypothesis of Alexander et al. [24] that mucin protects virions from environmental damage, as they concluded using infectivity assays with varying mucin concentrations in mouse hepatitis virus–containing droplets. Interestingly, it has been shown that virions co-localize with proteins for a large variety of viruses (from influenza to other coronaviruses [8, 12]). However, such studies were based on fluorescence microscopy with resolutions much larger than the size of individual viral particles. Thus, they cannot resolve whether this co-localization applies down to the virion, or to small aggregates of them. Our observations confirm that co-localization occurs at the scale of individual virions. Indeed, we do not see almost any virion that is not surrounded by, at least, a small amount of protein. The same applies to viral aggregates, which are always found in the presence of protein.

At large evaporation rates, i.e. at low humidity, more virions are found in the rim region and fewer in the central region. In contrast with the contact line region, virions in the central region tend to form smaller aggregates or even appear in isolation, as shown in Fig.1c. We also observe patches where the substrate is clear, indicating an absence of detectable protein. As stated above, virions located in these regions are still surrounded by a small amount of protein (Fig. 1c).

A third observation, common to both low and high humidity, is that a large fraction of the virions segregate from salt crystals (Fig. 17), as hypothesized by Morris and coauthors [1]. They associate to this segregation the slower decay rate of the infectivity observed after the drop fully evaporates.

The micrographs we have shown in this section are representative images of the residue, and similar ones have been obtained looking at other parts of this and other drops (see Suppl. Mat.). In this section we have focused on the results obtained for the composition with the smallest amount of protein, since they yield clearer micrographs and thus best convey the message. Nevertheless, the observations we report extend also to more physiological compositions.

Transport of solutes inside the drop

With the aim of clarifying the mechanisms behind the surprising viral distribution in shallow layers (mostly monolayers), we have carried out two sets of experiments: in the first one we aim to assess the spatio-temporal distribution of protein (mucin) as the drop evaporates, taking advantage of the natural fluorescence of mucin (FM, see Methods). In the second set, we measure the fluid velocity field inside the drop using two particle tracking velocimetry techniques: a two-dimensional one, allowing for more statistics in the middle section of the droplet, and a three-dimensional one, allowing for better precision on the particle trajectories in the vicinity of the interface (PTV, see Methods). In both sets of experiments, the droplets contained the same composition as those used in the TEM experiments, but using polymer-based tracer microparticles instead of virions. It is important to point out that we do not expect particles to interact between them as virions would do. The role of the particles here is to act a tracers to quantify the velocity field and the rate at which material from the bulk is captured at the receding droplet interface. In fact, to determine where and how virions are deposited the way they are in the residue of the dry drop, we look at the transport of protein since, as we showed above,

virions are always found in regions that contain protein.

The relative abundance of protein observed in the FM experiments reveals the existence of a net flow that transports material towards the rim. The existence of a net flow towards the rim in a sessile evaporating drop, termed capillary flow, is a well-known phenomenon firstly identified by Deegan and coworkers [25]. Such an evaporation-driven flow appears naturally due to a mismatch between the evaporative flux and a restricted contact-line motion, typically caused by contact-line pinning [26]. In order to maintain a spherical-cap shape and minimize the surface energy, a capillary liquid flow develops to replenish the contact line region. In the absence of other competing evaporation-driven flows, and for low-diffusivity solutes, the capillary flow concentrates non-volatile materials near the contact line and depletes the central region, leading to the so-called "coffee-ring effect" [26].

However, for drop compositions typical of respiratory fluids not all the material transported to the ring stays there, as it is evident in the FM experiments. In Fig. 2 we show three FM images taken at the beginning (left), middle (center), and end (right) of the evaporation process. Such a residue distribution is an indication that the capillary flow is not the only transport mechanism present in the evaporation of sessile respiratory droplets, and certainly not the one responsible for the observed viral distribution.

In 2a and b, before salt precipitates, the fluorescence emission is proportional to the total amount of protein along a drop vertical line [27, 28]. In 2a, at $t = 0$ s, we see that an incipient protein rim is forming, although a substantial amount of protein appears on the central region. In 2b, at $t = 240$ s, the rim is clearly visible and contains a much larger amount of protein than the central region as a consequence of the capillary flow. Interestingly, at the end of the evaporation process, when salt crystals form (rightmost panel), there is a large amount of salt in the central region. There is also enough protein to make the salt crystals fluorescent. The results for a drop that evaporates at 70% RH are qualitatively similar (SI, section).

The complex distribution of both solutes and virions is an indication that multiple evaporation-driven flows might be present within the sessile droplet, as well as other non-hydrodynamic effects. By adding fluorescent flow tracer particles and using appropriate illumination, one can clearly observe the particles following a toroidal-shaped vortex (Fig. 3a). This observation reveals the existence of a recirculatory flow with axial symmetry directed along the free surface from the droplet apex to the rim, and then back from the rim to the droplet center near the solid substrate. This later centerbound flow component contributes to mitigate the accumulation of solutes that would otherwise be generated close to the rim.

To explain the physical origin of the recirculation, we have put together a detailed mathematical model of the evaporation-induced flow inside the drop. The full description of the model can be found in the Supplementary Information, but we briefly highlight its main features here. We model the transport of water vapor in the air around the drop as purely diffusive. This leads to an inhomogeneous evaporation rate at the free surface that, thanks to the contact-line pinning, induces a flow inside the drop, slow enough to be dominated by viscous effects. This flow transports non-volatile solutes, mainly salt and protein, and other suspended material like virions. Owing to their large concentration, only salt and protein can influence the mass transport within the droplet. Therefore, we do not explicitly account for the transport of virions, as their concentration is too low to affect the flow. Moreover, their mutual interaction is not easily described mathematically. The mass transport equations both inside and outside the drop, as well as the Stokes equations inside the drop are integrated numerically in time using the finite-element software COMSOL 5.6.

The analysis of the simulations reveal that the high water evaporation rate near the rim makes this region rich in solutes specially in the case of protein, owing to its lower diffusivity (Fig. 2). This has several important effects. We start discussing the existence of the recirculation. On the one hand, the high salt concentration near the rim increases the surface tension coefficient. This creates a positive surface tension gradient along the free surface, from the drop apex to the contact line, which translates into a shear stress at the interface (also known as Marangoni stress) which drives a recirculatory flow with the same direction as the one we observe in the PTV experiments, and has been systematically observed in salt-rich evaporating sessile water droplets [29, 30, 22]. Due to their

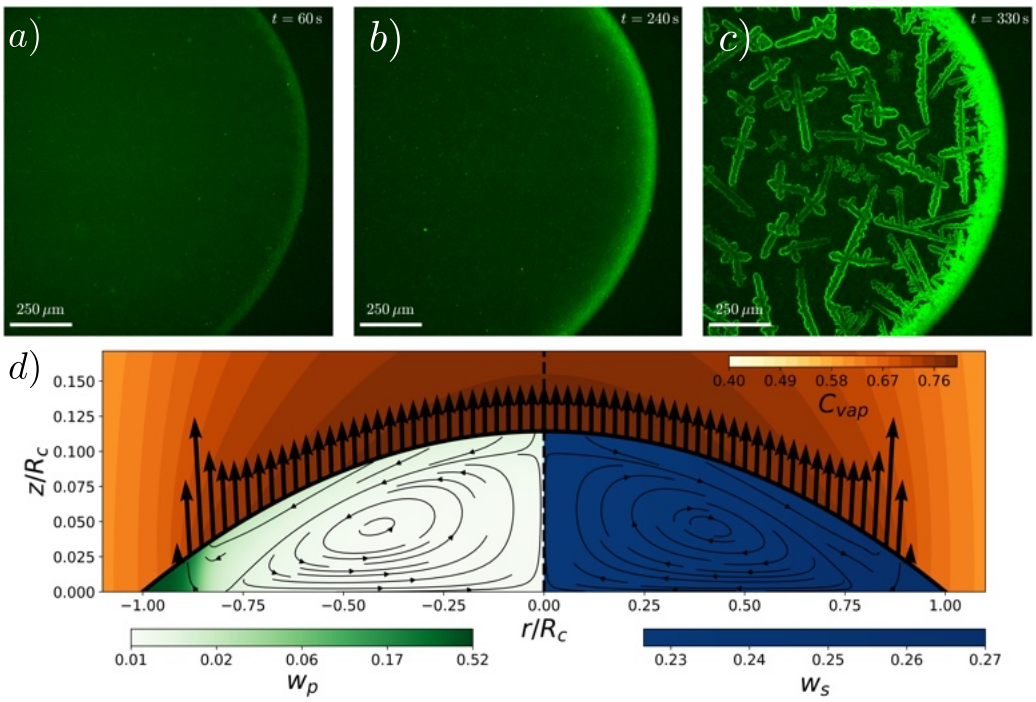

Figure 2: (a-c) Three instants during the drop evaporation process seen using fluorescence microscopy. From left to right, $t = 60, 240, 330$ s. The accumulation of protein near the rim is evident at t =240 s. At $t = 330$ s salt crystals have precipitated. The fact that they glow at the same wavelength as the protein suggests that they are coated by it. d) Snapshot of a numerical simulation right before salt saturation is reached at the contact line. The left side shows the protein concentration and the right one that of the salt. The arrows represent the local evaporation rate. The evaporated water vapor is transported by diffusion in the air, leading to a concentration field that is shown in yellow-orange color scale.

lower concentration, the other solutes present in the drop would generate a surface tension gradient smaller than that associated to the salt. On the other hand, since the liquid density increases with the solute concentration, evaporation induces a larger density near the drop interface, specially close to the rim. As a result, a buoyancy-driven recirculatory flow appears, which also moves fluid in the same direction as the one we observe in the PTV experiments. Since both, interfacial Marangoni stresses and buoyancy-driven forces, contribute to the resultant recirculating flow, a relevant question now is, for the drop sizes and composition used in this work, which one is the most dominant of these two effects on the observed flow? In our numerical simulations we can compute the effect of the density stratification without any free parameter, since the liquid density as a function of the protein and salt concentration can be readily taken from the literature [31]. In contrast, it is not possible to calculate the Marangoni stress *a priori*, since this would require knowing how the surface tension depends on the concentration field of surface active material at the droplet's free surface. This dependency is not easy to characterize experimentally, since tiny amounts of surface contaminants present in the environment, that are impossible to control, have a large impact on surface tension [32, 33, 26]. Consequently, our approach to solve this issue is to find numerically the intensity of the Marangoni flow –the Marangoni number– that best fits our experimentally measured using PTV (more details are given in the SI section). Interestingly, the values found of the Marangoni number are negligibly small, which suggests a negligible contribution of interfacial Marangoni forces to the observed flow pattern. If that is the case, and buoyancy-driven forces are the driving force behind the observed flow, then the direction in which gravity pulls the fluid would be determinant. To corroborate this finding, we conducted experiments with the substrate inclined at 20°, which clearly breaks the axial symmetry of the flow, confirming the importance of buoyancy-driven forces, Fig. 9. It is actually not surprising

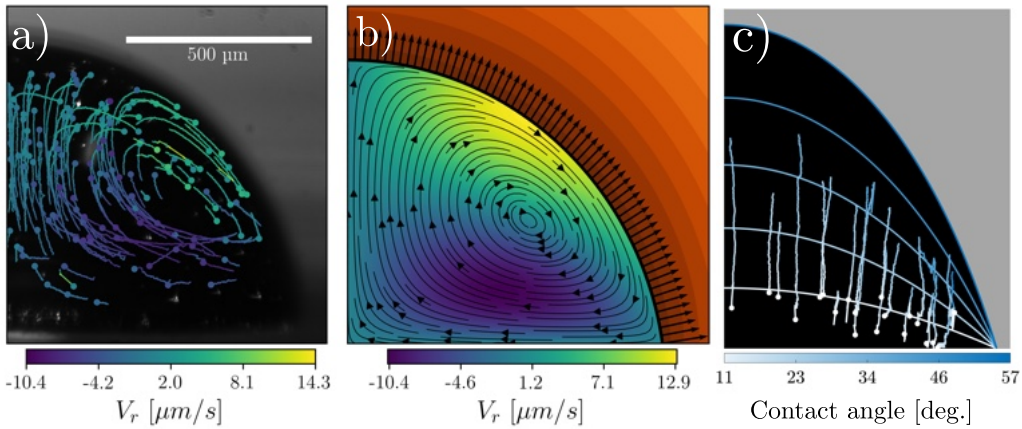

Figure 3: a) Snapshot of all the particle trajectories detected until $t = 750\,\mathrm{s}$ measured with particle tracking velocimetry for a drop evaporating at RH = 40%. b) numerical simulation corresponding to the same conditions and time as the experiment on the left panel. c) Particle trajectories (only those captured at the interface) and interface position detected with using a three-dimensional particle tracking technique for a drop evaporating at RH = 40%. We include additional images obtained with this 3D tracking technique in the Suppl. Information, Figs. 10 and 11.

to see that interfacial Marangoni stresses are hindered by contamination or other interfacial effects. There are multiple examples in the literature of such an effect, from pure evaporating sessile water droplets on thermally conducting substrates [34, 26], to rising bubbles in water [35]. In this particular case, the presence of the protein and surfactants *jams* the interface and hinder the appearance of a Marangoni surface stress. The same inhibition of Marangoni due to surface jamming has been observed for droplets containing a solution of albumin [36]. Careful experiments using passive colloidal probes at liquid interfaces have shown that traces amount of surfactant are enough to render the liquid interface incompressible, suppressing the development of surface stresses [37]. To conclude this argument, we would like to insist that the flow pattern but also the velocity values obtained numerically, in the absence of Marangoni stresses, compare remarkably well with experiments without fitting any free parameter (Figs. 3a and 3b).

During the droplet evaporation, a concentrated layer of solute is formed at the drying interface, specially faster at the contact line, where the evaporation flux is stronger. In fact, it can be proven mathematically that the evaporation rate for a droplet of a pure, volatile, liquid is actually infinite at the contact line [25]. To regularize this singularity, as we describe elsewhere [28], we incorporate the effect of the so-called water activity, χ, which quantifies how strongly water is retained by the protein matrix versus how available it is for diffusion and/or evaporation. In other words, it represents the ratio –always smaller than one– between the water vapor concentration at our droplet interface (containing proteins, salts and other solutes) and that corresponding to an interface of pure water. The same approach has been followed recently to explain the evaporation insensitivity of drying interfaces of supramolecular solutions [38, 39]. The model reflects the fact that water cannot reach the drop interface for large protein concentrations, since the mutual diffusion coefficient of the water-protein system decays very much for large protein concentrations [2]. In any case, the water activity decreases as the concentration of solutes at the interface increases, leading to a corresponding reduction in the local vapor concentration on the air side. The diffusive flux that drives evaporation, J, represented by the black arrows stemming from the drop surface in Figs. 3b and 2, is proportional to the difference between the vapor concentration at the interface and that far away from the drop, thus $J \sim \chi - H_r$. Consequently, a decrease in water activity reduces the local evaporation rate. For large relative humidity and solute concentration, this effect can even arrest evaporation altogether if the water activity equals the ambient relative humidity [4]. All in all, the reduction in the evaporation rate

slows the capillary flow near the rim. This effect is clearly seen in Fig. 2: the evaporation rate in the protein-rich region close to the rim is negligible compared to that near the center of the drop. We can also see how the maximum evaporation rate is no longer at the contact line, but displaced inwards to a region where the protein concentrations are low enough not to hinder evaporation. This explains why the protein rim, and the virions within, become more distributed than what they would be if all the material was concentrated at the contact line, as would be the case in a suspension of colloids in a pure liquid [25].

An interesting observation, which may have important implications for the viral infectivity, is that whereas protein concentrates mostly near the contact line forming a rim, salt crystals are more homogeneously distributed over the drop residue (Fig. 2c). This is a consequence of diffusion, which opposes to the accumulation of solutes near the contact line. In the case of salt, its diffusivity is still large enough to ensure a rather uniform concentration even at times close to full evaporation. Conversely, the diffusivity of protein is so low that diffusion cannot preclude the formation of the observed rim (Fig. 2). This conclusion is supported by the values of the Péclet numbers that can be estimated from the measured (and computed) values of the velocity. Using a characteristic velocity $V \approx 10\ 10\,\mu\mathrm{m\,s^{-1}}$, a drop footprint radius $R_c \approx 0.5\,\mathrm{mm}$, and the following values for the salt and protein diffusivity, $D_s = 2 \times 10^{-9}\ \mathrm{m^2\,s^{-1}}$ and $D_p = 5 \times 10^{-12}\ \mathrm{m^2\,s^{-1}}$ respectively [40, 41], we have $\mathrm{Pe_s} = 2.5$ and $\mathrm{Pe_p} = 10^3$. This confirms that the transport of protein is completely driven by advection, while the role of diffusion in the transport of salt cannot be neglected [28].

Discussion

We can draw some conclusions about the transport of virions inside the drop from the examination of the dry drop residue through TEM. We focus on the following observations: (a) virions organize preferentially in oligo- and monolayer aggregates, (b) the aggregates are located everywhere in the residue, but predominantly close to the contact line, specially at moderate or low humidity, and (c) these aggregates are found, with no exception, co-localized with mucin.

It is well known that virions form aggregates both in laboratory cultures and in their natural environment [42]. Among the factors that promote aggregation are the presence of salts [43] and organic materials [44] as well as a free surface [42], all of them elements found in evaporating sessile respiratory droplets. However, the morphology of these aggregates that we report here is more surprising. The observed organization of virions in shallow (often monolayer) aggregates, which are more abundant close to the contact line, resembles that of colloidal tracer particles seen in the residue of a sessile drop of a NaCl-water solution [22]. Bruning and coauthors showed that colloidal particles are captured by the free surface, which recedes due to the droplet evaporation.

Such a trapping effect can be clearly observed in our experiments using a three-dimensional particle tracking technique (GDPT [45, 46]) to track fluorescent polymer microparticles suspended in our evaporating sessile droplets containing protein and salts. This technique allows for simultaneous tracking of the particles and the droplet's free surface, and makes possible to find particles that are immobilized at the liquid-air interface. The results are shown in Figure 2c, which shows how particles tend to accumulate along the interface specially in the last stages of the evaporation process, when the contact angles are lowest. Once trapped at the surface, the recirculatory flow transports the particles towards the contact line region, where they aggregate. However, this transport along the interface is eventually arrested, as we discuss in the next paragraph. In the case of virions, it is reasonable to assume that the presence of organic non-volatile material at the interface, in particular proteins, further enhances aggregation. The fact that aggregation takes place to a big extent on a surface endows the aggregates with its two-dimensional nature. Notice that, were the aggregates formed in the bulk, they would be three-dimensional [47].

The capture at the interface, combined with the incompressibility of the liquid-air interface due to the large content in protein, explains the presence of viral aggregates everywhere in the dry residue. In fact, in Fig. 3c we see how captured particles end up following rather vertical trajectories, instead of following the recirculatory flow that dominates the motion in the bulk. This reveals that, after

some initial stage, the interface becomes incompressible due to the accumulation of protein. Interestingly, using only salt and a large concentration of colloids, Bruning et al. reported that at high salt and particle concentrations, aggregates are found extending all the way to the center of the drop residue [22]. Recently, a couple of studies [23, 8] have examined the distribution of fluorescently labeled coronaviruses by means of fluorescence microscopy. In both works, the authors found a large fluorescence signal in the central region of the drop, which they identify as virions. In the majority of these studies, the protein rim formation has been explained invoking the classical coffee-ring effect, where all the solutes are advected towards the contact line by the capillary flow [25]. Under the light of our experimental results and quantitative model, such explanation is not correct and misses many fundamental points.

Another important feature that we can observe thanks to our TEM technique is the presence of viral aggregates close to salt crystal structures. This can be explained as a fluid dynamical process: salt crystals nucleate when the solution becomes slightly supersaturated [48, 49]. At the onset of crystallization, the consumption of salt ions by the growing crystal reduces the saline concentration at its edges down to the saturation concentration, while the saline concentration remains supersaturated far away in the droplet bulk. This concentration gradient creates a flow towards the growing crystal, as reported by Efstratiou *et al.*, [50] (We also referred the reader to our supplementary movie 6). This flow advects protein, and also virions, towards the growing crystal.

Regardless of the proximity between viral aggregates and salt crystals, it has been proposed that they are protected from the salt's disinfectant effect by either being coated in mucin [1] or forming aggregates [42], whose nucleation and growth is also mediated by the presence of protein at the drop interface. In fact, all the virions that we can see in our experiments –either individuals or members of an aggregate– are located in regions that contain protein (Fig. 1 and Figs. S14, S13). This observation supports the mechanism put forward by Morris and coworkers [1], namely, at the end of the evaporation process salt and protein partition and segregate. Virions would be found mainly in protein-rich regions, far away from the damaging effect of the salt. To the best of our knowledge, it is the first time that this hypothesis has been verified experimentally, at least in what concerns the localization of virions.

In summary, in this work we have attempted to answer the question raised by Wilson Poon and coauthors in their seminal review article: "where are the virions in the respiratory droplets? The answer is poorly known at present" [6]. Moreover, to rationalize the observed viral distribution using TEM, we use a combination of fluorescence imaging, advanced microscopic tracking techniques and a precise mathematical modeling of the evaporation-driven transport within the sessile droplet. Understanding the evaporation-driven transport processes inside virus-laden respiratory droplets will allow researchers to clarify crucial open questions regarding disease transmission. In fact, the local microenvironment where virions rest determines the viral stability [15], and this microenvironment is ultimately shaped by the transport mechanisms that we elucidate in this article.

A few years ago, we experienced globally the devastating effects of viral airborne transmission during the COVID-19 pandemic. A natural continuation of this work would be to analyze the viral distribution in airborne droplets. However extending our experimental methodology to spherical airborne drops is far from trivial. Although there exist some notable experimental studies on the evaporation of such model respiratory drops [19, 3], current techniques do not allow for assessing virus distribution within these systems. Addressing this challenge is essential for advancing our understanding of airborne disease transmission.

The authors acknowledge financial support from Grant No. PID2023-146809OB-I00 funded by MICIU/AEI/10.13039/501100011033 and by ERDF/UE and Grant No. PID2020-114945RB-C21 funded by MCIN/AEI/10.13039/501100011033. We are indebted to Dr. Kevin Roger for his insightful comments about the segregation of components in the dry residue of the drop. We are also very thankful to Prof. Lorenzo Botto for his valuable suggestions on the topic of the formation of viral aggregates on the drop surface.

Materials and Methods

Culture of cells and viruses

Epithelial swine testis (ST) cells (ATCC CRL-1746), originally described by McClurkin *et al.* [51], were cultured at 37 °C in a humidified atmosphere with 5 % CO_2. Cells were maintained in Dulbecco's Modified Eagle Medium (DMEM) supplemented with 10 % fetal bovine serum (FBS), 1 mmol L^{-1} sodium pyruvate, 100 U/mL penicillin, 100 µg mL^{-1} streptomycin, 2 mmol L^{-1} glutamine, and 1 mmol L^{-1} non-essential amino acids (hereafter referred to as growth medium). The TGEV strain PUR-MAD [52] was kindly provided by L. Enjuanes (CNB-CSIC, Madrid, Spain). The virus was propagated in ST cells using growth medium supplemented with 2 % FBS and titrated by plaque assay on ST cells monolayers, as previously described [53, 54].

Virus purification

Highly purified TGEV was prepared as previously described [55]. Briefly, ST cells were infected with TGEV at a multiplicity of infection (MOI) of 1 plaque-forming unit (PFU) per cell. When the cytopathic effect (CPE) was apparent (36 h post-infection), the culture supernatants were harvested and clarified by centrifugation at 4500 *g* for 20 min at 4 °C. The virus was then concentrated by ultracentrifugation at 112000 *g* for 120 min at 4 °C through a 31 % (w/w) sucrose cushion in TEN buffer (10 mM Tris-HCl [pH 7.4], 1 mM EDTA, 1 M NaCl) with 0.2 % Tween 20 and subsequently purified over a continuous 30 % to 42 % sucrose density gradient (112000 *g* for 120 min at 4 °C). Finally, the purified virus was centrifuged at 112000 *g* for 60 min at 4 °C, resuspended in TNE buffer (10 mM Tris-HCl [pH 7.4], 1 mM EDTA, 100 mM NaCl), aliquoted and stored at −80 °C until use. Virus concentration and virus titre were determined by spectrophotometry and plaque assay, respectively. Finally, Purity and structural integrity of the viral preparation were confirmed by conventional electron microscopy, which showed that over 99 % of particles retained their morphology, with no detectable vesicles or other contaminants.

Drop compositions used in the TEM experiments

The artificial saliva is prepared following the composition used by Vejerano & Marr [5], namely milliQ water with 9 g/l of NaCl (Sigma-Aldrich), 3 g/l of porcine gastric mucin type III (Sigma-Aldrich) and 0.5 g/l of the pulmonar surfactant 1,2-dihex-adecanoyl-sn-glycero-3-phosphocholine.

Finally, the TNE used to suspend the purified viruses, is a buffer composed of 0.5 M NaCl, 1 mM EDTA, 20 mM Tris - HCl, and pH 7-5. Specifically, 9 µL of TGEV suspension (titre 1.27×10^9 TCDI50) are diluted in 21 µL of TNE to form the solution for the droplet.

The addition of paraformaldehyde to the solution is needed to inactivate the virions before the sample is taken to the electron microscope, which is located outside the biosafety lab.

Using these ingredients, we have prepared two solutions where the saliva has different levels of dilution:

- **Composition A (diluted):** 2.22 µL artificial saliva + 3 µL TGEV suspension + 1 µL Paraformaldehyde + 13.8 µL TNE.
- **Composition B (less diluted)**: 6.66 µL artificial saliva + 3 µL TGEV suspension + 1 µL Paraformaldehyde + 9.4 µL TNE.

Also, we have prepared to solutions equivalent to A and B, but where the suspension of viruses in TNE is replaced by just TNE. Drops of these compositions were used in control experiments:

- **Composition Blank A (diluted):** 2.22 µL artificial saliva + 1 µL Paraformaldehyde + 16.8 µL TNE.

- **Composition Blank B (less diluted)**: 6.66 µL artificial saliva + 1 µL Paraformaldehyde + 12.4 µL TNE.

Using these compositions, we have carried out the following experiments with droplets containing virions:

Exp. Number	Composition	Initial droplet size [µL]	Rel. Humidity (%)
1	A	0.67	40
2	A	0.25	40
3	A	0.32	40
4	B	0.41	40
5	B	0.17	40
6	B	0.35	40
7	A	0.15	70
8	A	0.4	70
9	A	0.18	70

Table 1: List of TEM experiments.

Drop evaporation and velocity field measurements

We deposit sessile respiratory-like droplets with an initial volume of $V_0 = 0.3 \pm 0.1$ µL onto a micropetri dish coated with a polymeric substrate. This dish, provided by IBIDI, enables high-resolution imaging and minimizes autofluorescence. Droplets evaporate inside a humidity-controlled chamber, based on the design by Boulogne [56]. The relative humidity (RH) was varied between 30% and 80%. Humid air is generated by recirculating air through a water bottle, while dry air is produced by passing it through a bottle containing Calcium Sulfate, a highly hygroscopic salt.

To measure the velocity field inside the evaporating droplets, we introduce glass hollow spherical tracer particles (Potters Sphericel 110P8) ensuring that the concentration remains low enough to avoid disturbing the flow (0.003 w/w%). Since the flow is experimentally observed to be axisymmetric, we track the particle positions within a meridional plane of the droplet. To achieve this, we illuminate the droplet from below using a thin laser sheet focused through a cylindrical lens. In particle tracking velocimetry (PTV) experiments, we record the droplet from the side. Given that the evaporation timescale is significantly longer than the velocity field timescale, we record particle motion at 1 fps and the droplet interface at 0.1 fps. To achieve this, we electrically control an LED light to switch on every 10 seconds, briefly illuminating the droplet's interface. The air–droplet interface refracts light traveling from the particles to the camera. Since the interface forms a spherical cap, this distortion can be corrected analytically. Using the experimentally determined interface shape, we apply ray-tracing corrections following the method of [57]. Although the velocity field remains qualitatively consistent throughout evaporation, refraction effects become significant when the droplet becomes very thin. Therefore, we analyze particle trajectories only until the contact angle decreases to approximately $\theta_c \sim 10°$.

To study the final stages of evaporation, we complement side-view PTV with dedicated experiments using General Defocusing Particle Tracking (GDPT) [45, 46]. Fluorescent polystyrene microparticles with 1 µm diameter (Microparticles GmbH) are introduced into the droplets and imaged from below using an inverted epifluorescence microscope (Nikon Eclipse Ti2). GDPT relies on optical systems with shallow depth of field, where particle defocusing correlates with depth position. A calibration set of images is used to build a lookup table that maps particle image shapes to depth. To enhance performance, GDPT is combined with a cylindrical lens that introduces astigmatism, causing spherical particles to appear elliptical. The ellipse shape varies with depth, enabling accurate 3D tracking.

Transmission Electron microscopy

Droplets of samples 0.3± 0.1 µL were adsorbed onto Formvar carbon-coated 200 mesh nickel grids (Electron Microscopy Sciences). Grids were left dry in humidity chamber at low (40 %) and high (70 %) RH as previously described. Unstained grids were visualised in a JEOL JEM 1400 Flash electron microscope (JEOL, Tokyo, Japan) operating at 100 kV 100 kV. No uranyl acetate staining was used to avoid dilution of salt crytals in aqueous solution. Micrographs were taken with a Gatan OneView digital camera (Gatan, California, USA) at various magnifications.

Fluorescence Microscope imaging parameters and methods

To study the spatial distribution of mucin and salt crystals during droplet evaporation, we prepared 0.3 µL droplets mimicking the composition of human saliva. The droplets were deposited onto μ-Dish 35 mm, high glass-bottom dishes (Ibidi) under ambient conditions. The composition of the droplets was identical to that used in parallel transmission electron microscopy (TEM) experiments. Evaporation dynamics were monitored using an inverted widefield fluorescence microscope (Leica DMi8) equipped with a CoolLED pE-4000 illumination system and an Orca-Flash 4.0 sCMOS camera (Hamamatsu). Images were acquired using a 10×/0.32 HC PL FLUO objective. Excitation was performed using a 405 nm LED set to 25 % power. The microscope was equipped with a quad-band fluorescence filter set (QUA), however, only the channel corresponding to excitation at 405 nm and emission collection at 420–480 nm was used in this study. Both mucin and salt crystals emit fluorescence within this spectral range upon 405 nm excitation, allowing simultaneous visualization of their distribution. The exposure time was set to 20 ms per acquisition. Droplet evaporation was imaged every 30 seconds for a total duration of 10 minutes, or until complete evaporation and residual pattern formation were observed.

References

[1] Dylan H Morris et al. "Mechanistic theory predicts the effects of temperature and humidity on inactivation of SARS-CoV-2 and other enveloped viruses". In: *Elife* 10 (2021), e65902.

[2] Tania Merhi et al. "Assessing suspension and infectivity times of virus-loaded aerosols involved in airborne transmission". In: *Proceedings of the National Academy of Sciences* 119.32 (2022), e2204593119.

[3] Henry P Oswin et al. "The dynamics of SARS-CoV-2 infectivity with changes in aerosol microenvironment". In: *Proceedings of the National Academy of Sciences* 119.27 (2022), e2200109119.

[4] Carola Seyfert et al. "Stability of respiratory-like droplets under evaporation". In: *Physical review fluids* 7.2 (2022), p. 023603.

[5] Eric P Vejerano and Linsey C Marr. "Physico-chemical characteristics of evaporating respiratory fluid droplets". In: *Journal of The Royal Society Interface* 15.139 (2018), p. 20170939.

[6] Wilson CK Poon et al. "Soft matter science and the COVID-19 pandemic". In: *Soft matter* 16.36 (2020), pp. 8310–8324.

[7] Qishen Huang, Wei Wang, and Peter J. Vikesland. "Implications of the Coffee-Ring Effect on Virus Infectivity". In: *Langmuir* 37.38 (2021), pp. 11260–11268. DOI: `10.1021/acs.langmuir.1c01610`.

[8] Zi-Meng Kong et al. "Virus dynamics and decay in evaporating human saliva droplets on fomites". In: *Environmental science & technology* (2022).

[9] Robert Groth et al. "Toward Standardized Aerovirology: A Critical Review of Existing Results and Methodologies". In: *Environmental Science & Technology* 58.8 (2024), pp. 3595–3608.

[10] Aline Schaub et al. "Salt-mediated inactivation of influenza A virus in 1-μl droplets exhibits exponential dependence on NaCl molality". In: *bioRxiv* (2023).

[11] Michael D Vahey and Daniel A Fletcher. "Influenza A virus surface proteins are organized to help penetrate host mucus". In: *Elife* 8 (2019), e43764.

[12] Jin Pan et al. "Mucin Colocalizes with Influenza Virus and Preserves Infectivity in Deposited Model Respiratory Droplets". In: *Environmental Science & Technology* (2025).

[13] Andrea J. French et al. "Environmental Stability of Enveloped Viruses Is Impacted by Initial Volume and Evaporation Kinetics of Droplets". In: *mBio* 14 (2023), e03452–22.

[14] Nicole C. Rockey et al. "Seasonal influenza viruses decay more rapidly at intermediate humidity in droplets containing saliva compared to respiratory mucus". In: *Applied and Environmental Microbiology* 90 (2024), e02010–23.

[15] Alexandra K Longest et al. "Review of factors affecting virus inactivation in aerosols and droplets". In: *Journal of the Royal Society Interface* 21.215 (2024), p. 20240018.

[16] Lakshmi Nathan and Susan Daniel. "Single virion tracking microscopy for the study of virus entry processes in live cells and biomimetic platforms". In: *Physical Virology: Virus Structure and Mechanics* (2019), pp. 13–43.

[17] Miguel Cantero et al. "Monitoring SARS-CoV-2 surrogate TGEV individual virions structure survival under harsh physicochemical environments". In: *Cells* 11.11 (2022), p. 1759.

[18] Xiaoyun Yang et al. "Immobilization of pseudorabies virus in porcine tracheal respiratory mucus revealed by single particle tracking". In: *PloS one* 7.12 (2012), e51054.

[19] Erik Huynh et al. "Evidence for a semisolid phase state of aerosols and droplets relevant to the airborne and surface survival of pathogens". In: *Proceedings of the National Academy of Sciences* 119.4 (2022), e2109750119.

[20] Patrick CY Woo et al. "ICTV Virus Taxonomy Profile: Coronaviridae 2023: This article is part of the ICTV Virus Taxonomy Profiles collection." In: *Journal of general virology* 104.4 (2023), p. 001843.

[21] Ella Hartenian et al. "The molecular virology of coronaviruses". In: *Journal of Biological Chemistry* 295.37 (2020), pp. 12910–12934.

[22] Myrthe A Bruning, Laura Loeffen, and Alvaro Marin. "Particle monolayer assembly in evaporating salty colloidal droplets". In: *Physical review fluids* 5.8 (2020), p. 083603.

[23] Casia L Wardzala et al. "Mucins inhibit coronavirus infection in a glycan-dependent manner". In: *ACS Central Science* 8.3 (2022), pp. 351–360.

[24] Robert W Alexander et al. "Mucin transiently sustains coronavirus infectivity through heterogenous changes in phase morphology of evaporating aerosol". In: *Viruses* 14.9 (2022), p. 1856.

[25] Robert D. Deegan et al. "Capillary flow as the cause of ring stains from dried liquid drops". In: *Nature* 389 (1997), pp. 827–829.

[26] Hanneke Gelderblom, Christian Diddens, and Alvaro Marin. "Evaporation-driven liquid flow in sessile droplets". In: *Soft matter* 18.45 (2022), pp. 8535–8553.

[27] Tadashi Kajiya*, Daisaku Kaneko, and Masao Doi. "Dynamical visualization of "coffee stain phenomenon" in droplets of polymer solution via fluorescent microscopy". In: *Langmuir* 24.21 (2008), pp. 12369–12374.

[28] Javier Martínez-Puig et al. "On the role of water activity on the formation of a protein-rich coffee ring in an evaporating multicomponent drop". In: *arXiv preprint arXiv:2509.09315* (2025).

[29] Virginie Soulié et al. "The evaporation behavior of sessile droplets from aqueous saline solutions". In: *Physical Chemistry Chemical Physics* 17.34 (2015), pp. 22296–22303.

[30] Álvaro Marín et al. "Solutal Marangoni flow as the cause of ring stains from drying salty colloidal drops". In: *Physical Review Fluids* 4 (2019), p. 041601.

[31] Antonios G. Mikos and Nikolaos A. Peppas. "Measurement of the surface tension of mucin solutions". In: *International Journal of Pharmaceutics* 53 (1989), pp. 1–5.

[32] A Ponce-Torres, EJ Vega, and JM Montanero. "Effects of surface-active impurities on the liquid bridge dynamics". In: *Experiments in Fluids* 57.5 (2016), p. 67.

[33] Duarte Rocha et al. "Evaporating sessile droplets: solutal Marangoni effects overwhelm thermal Marangoni flow". In: *Journal of Fluid Mechanics* 1013 (2025), A39. DOI: 10.1017/jfm.2025.10208.

[34] Hua Hu and Ronald G Larson. "Analysis of the effects of Marangoni stresses on the microflow in an evaporating sessile droplet". In: *Langmuir* 21.9 (2005), pp. 3972–3980.

[35] Harishankar Manikantan and Todd M Squires. "Surfactant dynamics: hidden variables controlling fluid flows". In: *Journal of fluid mechanics* 892 (2020), P1.

[36] Fan Du, Liyuan Zhang, and Wei Shen. "The internal flow in an evaporating human blood plasma drop". In: *Journal of Colloid and Interface Science* 609 (2022), pp. 170–178.

[37] Mehdi Molaei et al. "Interfacial flow around Brownian colloids". In: *Physical Review Letters* 126.22 (2021), p. 228003.

[38] Jean-Baptiste Salmon, Frédéric Doumenc, and Béatrice Guerrier. "Humidity-insensitive water evaporation from molecular complex fluids". In: *Phys. Rev. E* 96 (3 Sept. 2017), p. 032612. DOI: 10.1103/PhysRevE.96.032612. URL: https://link.aps.org/doi/10.1103/PhysRevE.96.032612.

[39] Max Huisman et al. "Evaporation of Concentrated Polymer Solutions Is Insensitive to Relative Humidity". In: *Phys. Rev. Lett.* 131 (24 Dec. 2023), p. 248102. DOI: 10.1103/PhysRevLett.131.248102. URL: https://link.aps.org/doi/10.1103/PhysRevLett.131.248102.

[40] Vincenzo Vitagliano and P. Lyons. "Diffusion Coefficients for Aqueous Solutions of Sodium Chloride and Barium Chloride". In: *Journal of the American Chemical Society* 78 (Apr. 1956). DOI: 10.1021/ja01589a011.

[41] Xingxiang Cao et al. "pH-Dependent Conformational Change of Gastric Mucin Leads to Sol-Gel Transition". In: *Biophysical Journal* 76 (1999), pp. 1250–1258.

[42] Charles P Gerba and Walter Q Betancourt. "Viral aggregation: impact on virus behavior in the environment". In: *Environmental science & technology* 51.13 (2017), pp. 7318–7325.

[43] Leonardo Gutierrez and Thanh H Nguyen. "Interactions between rotavirus and Suwannee River organic matter: aggregation, deposition, and adhesion force measurement". In: *Environmental science & technology* 46.16 (2012), pp. 8705–8713.

[44] Valesca Anschau and Rafael Sanjuán. "Fibrinogen gamma chain promotes aggregation of vesicular stomatitis virus in saliva". In: *Viruses* 12.3 (2020), p. 282.

[45] Rune Barnkob, Christian J. Kähler, and Massimiliano Rossi. "General defocusing particle tracking". In: *Lab Chip* 15 (17 2015), pp. 3556–3560.

[46] Rune Barnkob and Massimiliano Rossi. "DefocusTracker: A Modular Toolbox for Defocusing-based, Single-Camera, 3D Particle Tracking". In: *Journal of Open Research Software* 9.1 (2021), p. 22.

[47] Devendra Pal et al. "Real-time 4D tracking of airborne virus-laden droplets and aerosols". In: *Communications Engineering* 2.1 (2023), p. 41.

[48] Julie Desarnaud et al. "Metastability Limit for the Nucleation of NaCl Crystals in Confinement". In: *The Journal of Physical Chemistry Letters* 5 (2014), pp. 890–895.

[49] Julie Desarnaud et al. "Hopper Growth of Salt Crystals". In: *The Journal of Physical Chemistry Letters* 9 (2018), pp. 2961–2966.

[50] Marina Efstratiou, John Christy, and Khellil Sefiane. "Crystallization-Driven Flows within Evaporating Aqueous Saline Droplets". In: *Langmuir* 36 (2020), pp. 4995–5002.

[51] AW McClurkin and James O Norman. "Studies on transmissible gastroenteritis of swine: II. Selected characteristics of a cytopathogenic virus common to five isolates from transmissible gastroenteritis". In: *Canadian Journal of Comparative Medicine and Veterinary Science* 30.7 (1966), p. 190.

[52] Carlos M Sánchez et al. "Antigenic homology among coronaviruses related to transmissible gastroenteritis virus". In: *Virology* 174.2 (1990), pp. 410–417.

[53] G Jiménez et al. "Critical epitopes in transmissible gastroenteritis virus neutralization". In: *Journal of Virology* 60.1 (1986), pp. 131–139.

[54] Carlos M Sánchez et al. "Genetic evolution and tropism of transmissible gastroenteritis coronaviruses". In: *Virology* 190.1 (1992), pp. 92–105.

[55] Aitor Nogales et al. "Transmissible gastroenteritis coronavirus RNA-dependent RNA polymerase and nonstructural proteins 2, 3, and 8 are incorporated into viral particles". In: *Journal of virology* 86.2 (2012), pp. 1261–1266.

[56] François Boulogne. "Cheap and versatile humidity regulator for environmentally controlled experiments". In: *The European Physical Journal E* 42 (2019), pp. 1–4.

[57] Kwan Hyoung Kang et al. "Quantitative visualization of flow inside an evaporating droplet using the ray tracing method". In: *Measurement Science and Technology* 15.6 (2004), p. 1104. DOI: 10.1088/0957-0233/15/6/009.

[58] E Mikhailov et al. "Interaction of aerosol particles composed of protein and saltswith water vapor: hygroscopic growth and microstructural rearrangement". In: *Atmospheric Chemistry and Physics* 4.2 (2004), pp. 323–350.

[59] Yana Znamenskaya et al. "Effect of Hydration on Structural and Thermodynamic Properties of Pig Gastric and Bovine Submaxillary Gland Mucins". In: *The Journal of Physical Chemistry B* 116 (2012), pp. 5047–5055. DOI: 10.1021/jp212495t.

[60] Antonios G. Mikos and Nikolaos A. Peppas. "Measurement of the surface tension of mucin solutions". In: *International Journal of Pharmaceutics* 53.1 (1989). DOI: https://doi.org/10.1016/0378-5173(89)90354-2.

[61] Christian Diddens, Yaxing Li, and Detlef Lohse. "Competing Marangoni and Rayleigh convection in evaporating binary droplets". In: *Journal of Fluid Mechanics* 914 (2021). DOI: 10.1017/jfm.2020.734.

[62] Abdur Rasheed et al. "Precipitation dynamics of surrogate respiratory sessile droplets leading to possible fomites". In: *Journal of Colloid and Interface Science* 600 (2021), pp. 1–13.

[63] Amey Nitin Agharkar et al. "Evaporation of bacteria-laden surrogate respiratory fluid droplets: On a hydrophilic substrate vs contact-free environment confers differential bacterial infectivity". In: *Physics of Fluids* 36 (2024), p. 031912.

[64] Michael P. Adams et al. "Ice nucleation by viruses and their potential for cloud glaciation". In: *Biogeosciences* 18 (2021), pp. 4431–4444.

Supplemental Information

Hydrodynamical and transport model

The axial symmetry of the problem allows us to formulate the equations in axisymmetric cylindrical coordinates, where Ω_G and Ω_D denote the gas and droplet phases, respectively. The domain boundaries are the substrate Γ_{Sub}, the axis of symmetry Γ_{Sym}, the far-field Γ_F, and the gas–droplet interface Γ_I.

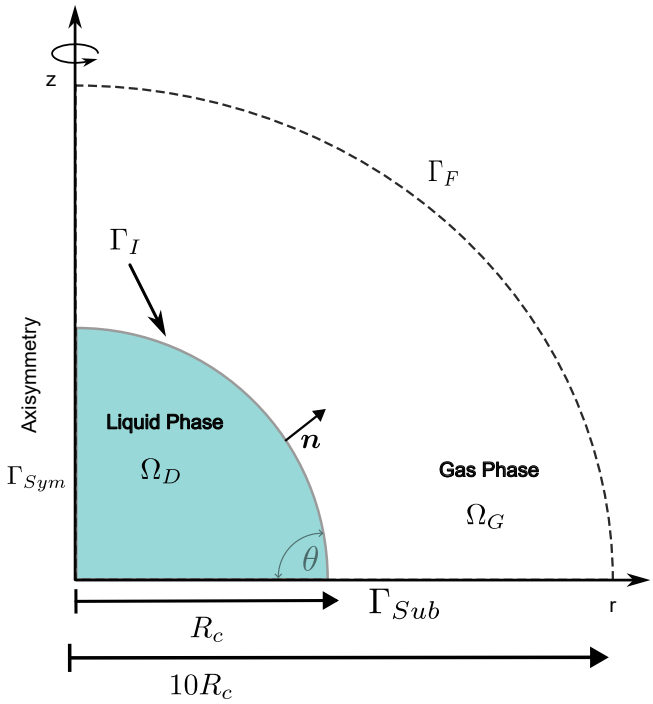

Figure 4: Sketch of the numerical domain.

Transport model in the gas phase

In the gas phase we consider the diffusion-driven transport of vapor from the droplet into the air. When the droplet evaporates at a temperature far below the boiling point, and in the absence of forced or strong natural convection, the transport in the gas phase can be considered purely diffusive. Also, the evolution of the vapor concentration field can be treated as quasi-stationary since the diffusive time scale $D_{vap}/R_c^2 \sim 10^{-1}$ s is several orders of magnitude smaller than the droplet drying time $\rho_0 V_0/(4R_c D_{vap} C_s(1-H_r)) \sim 10^2$ s. Here, V_0 is the initial drop volume, ρ_0 the (constant) liquid density, D_{vap} the diffusivity of water vapor in air, C_s the saturation concentration, and H_r the relative humidity.

Under the above assumptions, the equation for the transport of vapor in the air reduces to the Laplacian

$$\nabla^{2*} C^*_{vap} = 0 \text{ at } \Omega_G. \tag{1}$$

We use $*$ to denote the dimensional water vapor concentration and Nabla operator. We describe now the boundary conditions to integrate this equation. At the substrate and the symmetry axis we impose no flux of vapor:

$$\boldsymbol{\nabla}^* C^*_{vap} \cdot \boldsymbol{n} = 0 \text{ at } \Gamma_{Sub} \cup \Gamma_{Sym} \tag{2}$$

At the interphase between the liquid and the gas, thermodynamic equilibrium imposes

$$C^*_{vap} = C_s\,\chi(w_s, w_p) \text{ at } \Gamma_I. \tag{3}$$

Here, χ is the water activity that depends on the salt and protein mass fraction w_s and w_p. To model the water activity we assume $\chi(w_s, w_p) = \chi_s(w_s) + \chi_p(w_p) - 1$ and we interpolate the experimental obtained by Mikhailov and coauthors [58] for χ_s, and by Znamenskaya and coworkers [59] for χ_p.

Far away from the droplet we have

$$C^*_{vap} = C_s\,H_r \text{ at } \Gamma_F \tag{4}$$

We use the vapor saturation concentration C_s to nondimensionalize the vapor concentration C^*_{vap}. Doing so, the dimensionless equations for the transport of vapor in air result:

$$\begin{aligned}
\nabla^2 C_{vap} &= 0 \text{ at } \Omega_G && (5)\\
\boldsymbol{\nabla} C_{vap}\cdot\boldsymbol{n} &= 0 \text{ at } \Gamma_{Sub}\cup\Gamma_{Sym} && (6)\\
C_{vap} &= \chi(w_s, w_p) \text{ at } \Gamma_I && (7)\\
C_{vap} &= H_r \text{ at } \Gamma_F. && (8)
\end{aligned}$$

Notice that we omit the $*$ in the dimensionless versions of ∇^* and C^*_{vap}. Then the evaporation rate can be computed as

$$\boldsymbol{J} = -D\lambda\boldsymbol{\nabla} C_{vap} \tag{9}$$

where $\lambda = C_s/\rho_0$ and $D = D_{vap}/D_s$, and D_s is the diffusivity of salt in water. The choice of $J_c = \rho D_s/R_c$ to non-dimensionalize the evaporation rate will be justify later.

Transport of salt and protein inside the liquid phase

We will characterize the composition field using the mass fractions, w_w, w_s, and w_p, where the subindexes stand respectively for water, salt and protein. Since these three mass fractions must obey $w_w + w_s + w_p = 1$, we need to write advection-diffusion transport equations for only two of them, namely salt and protein.

We have the two following advection-diffusion transport equations for salt and protein:

$$\partial_{t^*} w_p + \boldsymbol{v^*}\cdot\boldsymbol{\nabla}^* w_p = D_p \nabla^{2^*} w_p \tag{10}$$

$$\partial_{t^*} w_s + \boldsymbol{v^*}\cdot\boldsymbol{\nabla}^* w_s = D_s \nabla^{2^*} w_s. \tag{11}$$

We present now the boundary conditions for these two equations. At the substrate and at the symmetry axis we have a no-flux boundary condition

$$\boldsymbol{\nabla}^* w_p\cdot\boldsymbol{n} = 0 \text{ at } \Gamma_{Sym}\cup\Gamma_{Sub} \tag{12}$$

$$\boldsymbol{\nabla}^* w_s\cdot\boldsymbol{n} = 0 \text{ at } \Gamma_{Sym}\cup\Gamma_{Sub}. \tag{13}$$

At the drop-air interphase the water mass flux must balance the evaporation rate computed by solving the vapor transport at the air side, $J^* = \boldsymbol{J^*}\cdot\boldsymbol{n}$:

$$w_w(\boldsymbol{v}^* - \boldsymbol{v_I}^*)\cdot\boldsymbol{n} - \boldsymbol{J}^*_w\cdot\boldsymbol{n} = \frac{J^*}{\rho_0} \text{ at } \Gamma_I, \tag{14}$$

where $\boldsymbol{v_I}^*$ is the velocity of the drop free surface. Moreover, since the concentration of salt and protein in the gas phase is zero,

$$\begin{aligned}
w_p(\boldsymbol{v}^* - \boldsymbol{v_I}^*)\cdot\boldsymbol{n} - D_p\boldsymbol{\nabla}^* w_p\cdot\boldsymbol{n} &= 0 \text{ at } \Gamma_I && (15)\\
w_s(\boldsymbol{v}^* - \boldsymbol{v_I}^*)\cdot\boldsymbol{n} - D_s\boldsymbol{\nabla}^* w_s\cdot\boldsymbol{n} &= 0 \text{ at } \Gamma_I. && (16)
\end{aligned}$$

We can sum the three boundary conditions and, using $w_w + w_s + w_p = 1$ once more and that the diffusive mass fluxes must sum zero, we arrive to the kinematic boundary condition

$$(\boldsymbol{v^*} - \boldsymbol{v_I^*}) \cdot \boldsymbol{n} = \frac{J^*}{\rho_0} \text{ at } \Gamma_I. \tag{17}$$

This equation will be used to solve for the evaporation-driven normal component of the interphase velocity, $\boldsymbol{v_I}^*$. It also lets us rewrite the boundary conditions for salt and protein mass fractions at the interphase as

$$D_p \boldsymbol{\nabla}^* w_p \cdot \boldsymbol{n} = \frac{J^* w_p}{\rho_0} \text{ at } \Gamma_I \tag{18}$$

$$D_s \boldsymbol{\nabla}^* w_s \cdot \boldsymbol{n} = \frac{J^* w_s}{\rho_0} \text{ at } \Gamma_I. \tag{19}$$

To nondimensionalize our equations we choose

$$\boldsymbol{x} = \frac{\boldsymbol{x^*}}{R_c},\ \boldsymbol{v} = \boldsymbol{v}^* \frac{R_c}{D_s},\ t = t^* \frac{D_s}{R_c^2}. \tag{20}$$

Now we can justify the choice of $J_c = \rho D_s / R_c$ because it leads to a kinematic boundary condition free of parameters,

$$(\boldsymbol{v} - \boldsymbol{v_I}) \cdot \boldsymbol{n} = J. \tag{21}$$

Applying the proposed non-dimensionalization to the rest of equations and boundary conditions we have

$$\partial_t w_p + \boldsymbol{v} \cdot \boldsymbol{\nabla} w_p = \mathcal{D} \nabla^2 w_p \text{ at } \Omega_D \tag{22}$$

$$\partial_t w_s + \boldsymbol{v} \cdot \boldsymbol{\nabla} w_s = \nabla^2 w_s \text{ at } \Omega_D \tag{23}$$

$$\boldsymbol{\nabla} w_p \cdot \boldsymbol{n} = 0 \text{ at } \Gamma_{Sym} \cup \Gamma_{Sub} \tag{24}$$

$$\boldsymbol{\nabla} w_s \cdot \boldsymbol{n} = 0 \text{ at } \Gamma_{Sym} \cup \Gamma_{Sub} \tag{25}$$

$$\boldsymbol{\nabla} w_p \cdot \boldsymbol{n} = \frac{J\, w_p}{\mathcal{D}} \text{ at } \Gamma_I \tag{26}$$

$$\boldsymbol{\nabla} w_s \cdot \boldsymbol{n} = J w_s \text{ at } \Gamma_I. \tag{27}$$

We have introduced the diffusivity ratio $\mathcal{D} = D_p / D_s$.

Hydrodynamic equations

In what follows, we will denote the composition-dependent liquid density by ρ^*. The evolution of the density is given by the continuity equation

$$\partial_{t^*} \rho^* + \boldsymbol{\nabla^*} \cdot (\rho^* \boldsymbol{v^*}) = 0 \tag{28}$$

Until this moment we have considered the density as a constant, ρ_0 but, in fact, the density depends on the composition. That is, on the mass fractions w_s and w_p. For dilute solutions, the density can be modeled as a linear function of both mass fractions [60]:

$$\rho^* = \rho_0 + \Delta\rho^* = \rho_0 + \rho_s w_s + \rho_p w_p. \tag{29}$$

However, since $\Delta\rho^*/\rho_0 \ll 1$ we just retain the term ρ_0 in all the previous equations. An exception to this is the gravity term in the momentum equation.Taking the density as constant everywhere except in the gravity term is called the Boussinesq approximation, solutal Boussinesq approximation in our case. As an example of why we have been able to neglect density variations in the previous equations, let us explain the non-dimensionalization of the continuity equation. Using the same non-dimensionalization for the time, length (and thus velocity) used before, continuity reads

$$\partial_t(\rho_0 + \rho_s w_s + \rho_p w_p) + \boldsymbol{\nabla} \cdot ((\rho_0 + \rho_s w_s + \rho_p w_p)\boldsymbol{v}) = 0 \tag{30}$$

Dividing by ρ_0 we have that

$$\partial_t \left(1 + \frac{\rho_s w_s + \rho_p w_p}{\rho_0}\right) + \boldsymbol{\nabla} \cdot \left(\left(1 + \frac{\rho_s w_s + \rho_p w_p}{\rho_0}\right)\boldsymbol{v}\right) = 0 \tag{31}$$

Then as $(\rho_s w_s + \rho_p w_p)/\rho_0 \ll 1$ during the whole evaporation,

$$\boldsymbol{\nabla} \cdot \boldsymbol{v} = 0. \tag{32}$$

We have arrived at the continuity equation of an incompressible flow which is typical of the Boussinesq approximation.

The momentum equation for an incompressible fluid reads

$$\rho^*(\partial_t \boldsymbol{v^*} + \boldsymbol{v^*} \cdot \boldsymbol{\nabla^*} \boldsymbol{v^*}) = -\boldsymbol{\nabla^*} p^* + \boldsymbol{\nabla^*} \cdot (\mu^*(\boldsymbol{\nabla} \boldsymbol{v^*} + \boldsymbol{\nabla} \boldsymbol{v^*}^T)) - \rho^* g \boldsymbol{e_z}. \tag{33}$$

Our non-dimensionalization, consistent with the one already used in the previous subsections, will be

$$t = \frac{D_s}{R_c^2} t^*,\ \boldsymbol{x} = \frac{\boldsymbol{x^*}}{R_c},\ \boldsymbol{v} = \boldsymbol{v}^* \frac{R_c}{D_s},\ \mu = \frac{\mu^*}{\mu_w},\ P = \frac{R_c^2}{\mu_w D_s}(p^* + \rho_0 g z^*) \tag{34}$$

where μ_w is the viscosity of pure water and P is the dimensionless reduced pressure. The characteristic pressure $\Delta p_c = \mu_w D_s / R_c^2$ has been chosen because the pressure gradient should be of the same order than the viscous stresses. Applying the non-dimensionalitation we have

$$\begin{aligned} \frac{(\rho_0 + \rho_s w_s + \rho_p w_p) D_s}{\mu_w} (\partial_t \boldsymbol{v} + \boldsymbol{v} \cdot \boldsymbol{\nabla} \boldsymbol{v}) = \\ -\boldsymbol{\nabla} P + \nabla \cdot (\mu(\boldsymbol{\nabla} \boldsymbol{v} + \boldsymbol{\nabla} \boldsymbol{v}^T)) - \frac{R_c^3 g}{\mu_w D_s}(\rho_s w_s + \rho_p w_p) g \boldsymbol{e_z}. \end{aligned} \tag{35}$$

Applying again $\Delta\rho^*/\rho_0 \ll 1$ we have

$$Sc^{-1}(\partial_t \boldsymbol{v} + \boldsymbol{v} \cdot \boldsymbol{\nabla} \boldsymbol{v}) = -\boldsymbol{\nabla} P + \boldsymbol{\nabla} \cdot (\mu(\boldsymbol{\nabla} \boldsymbol{v} + \boldsymbol{\nabla} \boldsymbol{v}^T)) - Ra\, \rho\, \boldsymbol{e_z}, \tag{36}$$

where $Sc = \mu_w / D_s \rho_0$ is the Schmidt number, $Ra = R_c^3 g \rho_s / \mu_w D_s$ the Rayleigh number, and $\rho = (w_s + \rho_p/\rho_s\, w_p)$ a dimensionless density variation. For our problem, $Sc > 10^3$, but we can only neglect inertia if the Reynolds number $Re = \rho_0 v_c R_c / \mu_w$ is also small, which is the case in our experiments where $v_c \approx 10\ \mu m$ and thus $Re \approx 10^{-2}$. In contrast with this $Ra \sim 10^6$ so we should keep buoyancy forces in the equations. This is the reason why we have applied the solutal Boussinesq approximation: changes in density are only relevant in the buoyancy forces, which only appear in the momentum equation. Finally, the dimensionless momentum equation reads

$$\boldsymbol{\nabla} \cdot \tau - Ra\, \rho\, \boldsymbol{e_z} = 0, \tag{37}$$

where $\tau = -P\mathcal{I} + \mu(\boldsymbol{\nabla} \boldsymbol{v} + \boldsymbol{\nabla} \boldsymbol{v}^T)$ is the dimensionless stress tensor defined using the reduced pressure P.

At the symmetry axis we impose symmetry conditions

$$v_r = 0,\ \frac{\partial v_z}{\partial r} = 0 \text{ at } \Gamma_{Sym}. \tag{38}$$

At the substrate we have no slip boundary condition

$$\boldsymbol{v} = 0 \text{ at } \Gamma_{Sub}. \tag{39}$$

At the interphase we have the kinematic boundary condition already derived in the previous subsection which in dimensionless form results

$$(\boldsymbol{v} - \boldsymbol{v_I}) \cdot \boldsymbol{n} = J, \text{ at } \Gamma_I. \tag{40}$$

This equation is needed to compute the interphase as part of our solution. However, this condition only gives the normal component of the interphase velocity, so another equation is needed that includes the tangential velocity component. This is going to be the stress condition

$$-\tau^* \cdot \boldsymbol{n} = \gamma^*(\boldsymbol{\nabla}^* \cdot \boldsymbol{n})\boldsymbol{n} - \boldsymbol{\nabla_t}^* \gamma^* + \rho_0 g z^* \boldsymbol{n}. \tag{41}$$

We assume that surface tension depends linearly on the concentration of salt $\gamma^* = \gamma_0 + \gamma_s w_s$. Then in dimensionless form the stress condition is

$$-\tau \cdot \boldsymbol{n} = Ca^{-1}((1 + CaMaw_s)\boldsymbol{\nabla} \cdot \boldsymbol{n} + Bo\, z)\boldsymbol{n} - Ma\boldsymbol{\nabla_t} w_s. \tag{42}$$

where $Ca = \mu_w D_s / \gamma_0 R_c$ is the capillary number, $Ma = \gamma_s R_c / \mu_w D_s$ the Marangoni number, and $Bo = \rho g R_c^2 / \gamma_0$ the Bond number.

To summarize, the hydrodynamic equations in the droplet are

$$\boldsymbol{\nabla} \cdot \boldsymbol{v} = 0, \text{ at } \Omega_D. \tag{43}$$

$$\boldsymbol{\nabla} \cdot \tau - Ra\, \rho\, \boldsymbol{e_z} = 0, \text{ at } \Omega_D \tag{44}$$

$$v_r = 0, \ \frac{\partial v_z}{\partial r} = 0 \text{ at } \Gamma_{Sym} \tag{45}$$

$$\boldsymbol{v} = 0, \text{ at } \Gamma_{Sub} \tag{46}$$

$$(\boldsymbol{v} - \boldsymbol{v_I}) \cdot \boldsymbol{n} = J, \text{ at } \Gamma_I \tag{47}$$

$$-\tau \cdot \boldsymbol{n} = Ca^{-1}((1 + CaMaw_s)\boldsymbol{\nabla} \cdot \boldsymbol{n} + Boz)\boldsymbol{n} - Ma\boldsymbol{\nabla_t} w_s \text{ at } \Gamma_I. \tag{48}$$

An scheme of the model can be seen in Fig. 5.

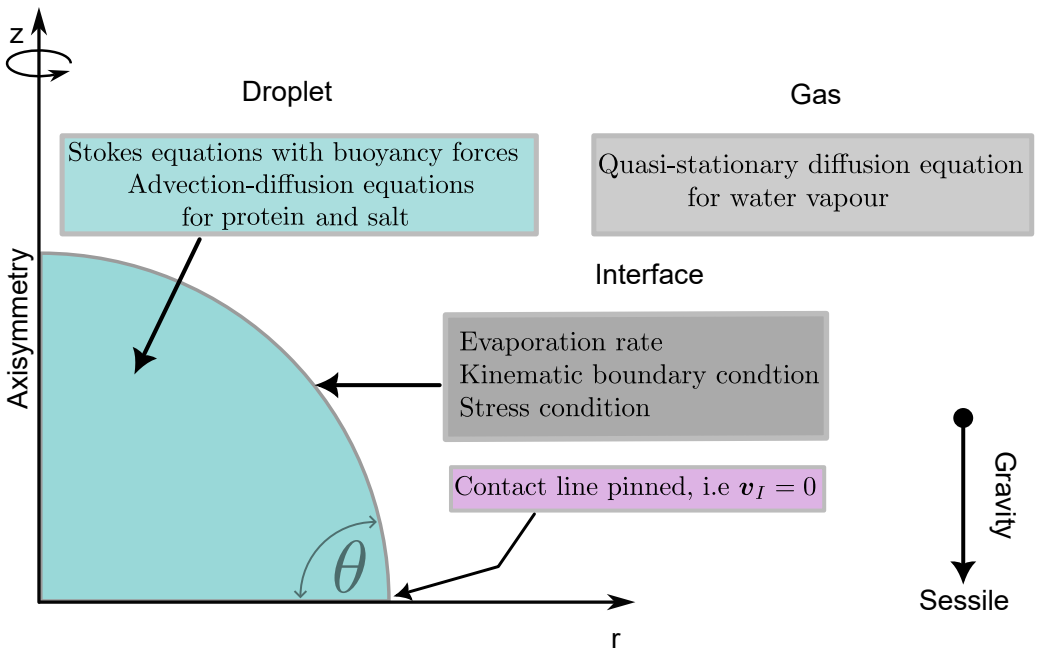

Figure 5: Sketch of the model, detailing which equations are applied in the different domains and boundaries.

This model accounts for the complexity of a respiratory droplet but has been kept as general as possible. Indeed it can be useful to study other ternary mixture droplets, where the solutal Boussinesq

approximation can be applied $\Delta\rho^*/\rho^* \ll 1$ and inertia can be neglected. This happens in a wide variety of applications [61]. The particularities of the system can be introduced via the dimensionless viscosity and density, and the dimensionless numbers. As explained in the main text the Marangoni number was set to 0 in the simulations.

Numerical scheme

To solve the model, we rewrite all dimensionless equations in weak form for implementation in COMSOL Multiphysics using the Mathematics Module. The incompressible Stokes flow with buoyancy forces is spatially discretized using Taylor–Hood triangular elements for velocity and pressure. Mesh deformation due to interfacial motion is handled with the Arbitrary Lagrangian–Eulerian (ALE) method. Time integration is performed using a variable-step, variable order backward differentiation formula (BDF) method of order 2 to 4, with adaptive step size to meet a relative tolerance of 10^{-4}.

Experimental Velocity Field

PTV: Side View

In the main text, we presented particle tracking results for composition Blank A at RH=40%. To complement this, we include experiments for compositions Blank B (see Fig. 6) and Blank A (see Fig. 7) at the same relative humidity. The higher protein content in these compositions reduces particle visibility, resulting in fewer detected particles and shorter trajectories. Despite this, a recirculatory flow is still observed, with characteristic velocities identical to those in composition Blank A.

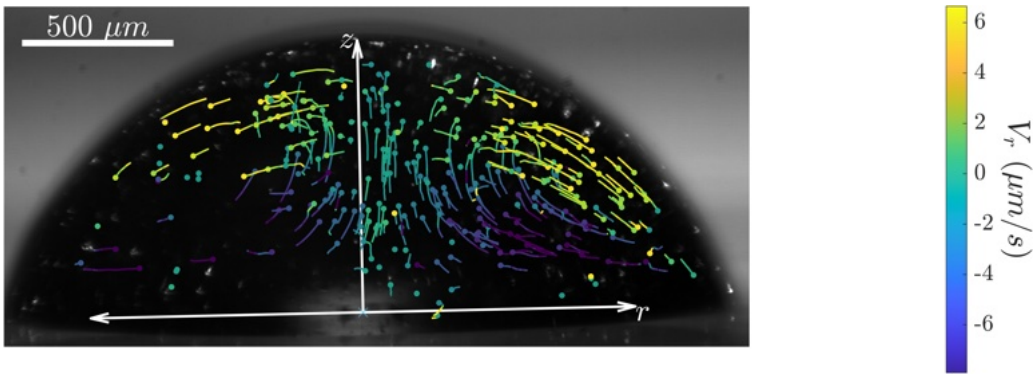

Figure 6: PTV of a droplet of composition Blank B evaporated at RH=40%

Additional particle tracking velocimetry (PTV) experiments were performed at RH=70% (see Fig. 8). In this case, the recirculatory flow persists but with lower velocities compared to the RH=40% condition. This is consistent with the hydrodynamic framework presented in the main text, and studied in more detail in Ref. [28]. The slower evaporation rate found at higher humidity translates into slower velocities inside the drop. Also, the distribution of solutes is more uniform, which smoothens up the density gradient that drives the recirculatory flow.

Finally, to verify that natural convection is the primary mechanism driving the recirculation, we conducted additional experiments in which the droplet was tilted by 20° relative to the direction of gravity. This tilt clearly breaks the flow symmetry (see Fig. 9), and the recirculation cells become approximately separated by the vertical (the direction of gravity), further supporting that the flow is buoyancy-driven.

GDPT: Particle capture at the interface

We show here two more images showing particle velocities obtained with the GDPT technique. In figure 10 we show the particle trajectories obtained during a first stage of the drop evaporation process.

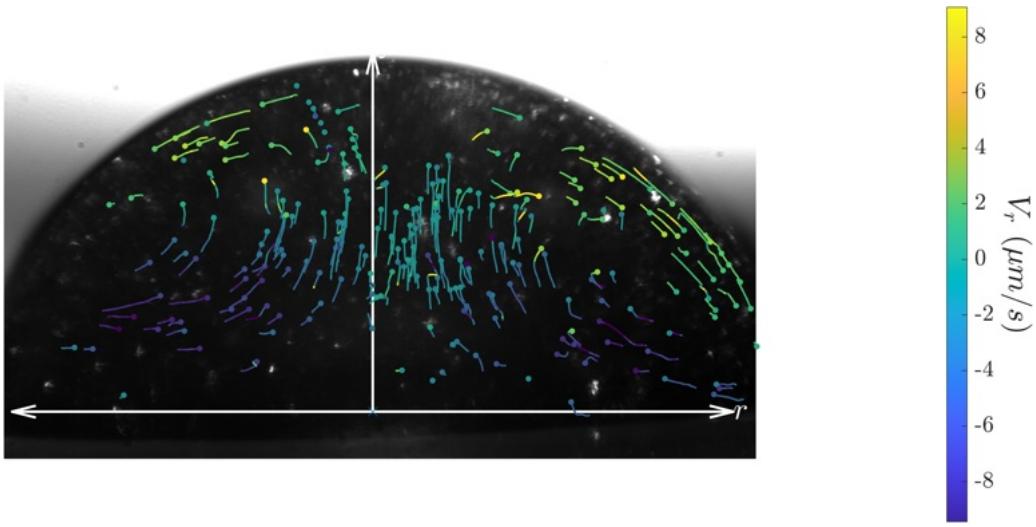

Figure 7: PTV of a droplet of composition Blank A evaporated at RH=40%

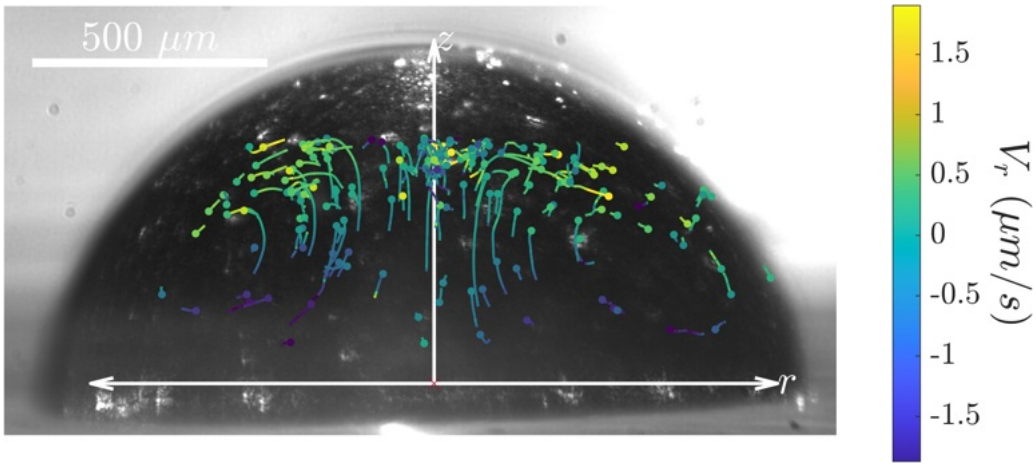

Figure 8: PTV of a droplet of composition Blank A evaporated at RH=70%

For times $t \leq 63$ s, the interface has not receded enough to capture a large amount of particles. Thus, they remain in the bulk. If the same analyses is repeated at later times, we see that several tracer particles have been captured by the receding interface. Remarkably, particles trapped at the surface do not follow the recirculatory flow observed in the bulk. This reveals that the interface is jammed with protein and other solutes.

Fluorescence Experiments

We also conducted fluorescence imaging experiments on droplets evaporated at RH=70% (see Fig. 12). Notably, within the timescale of the experiment, no crystallization was observed, in contrast to droplets evaporated at RH=40%. Additionally, the protein rim is significantly wider under these conditions. The contrast between the center of the droplet and the contact line is also less pronounced at RH=70%, indicating a lower peak protein concentration within the rim compared to the RH=40% case.

TEM images residues

In the main text, we present TEM images for the more diluted composition A. In order to show the reproducibility of our results we show more images of the dry residue of this composition at the contact line (see Fig. 13) and at the center (see Fig. 14). Fig. 15 shows corresponding TEM images for composition B, which contains three times more protein. In this case, visualization near

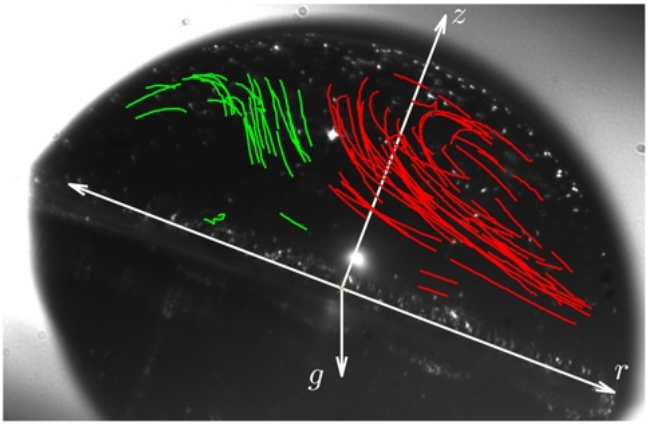

Figure 9: PTV of a tilted droplet of composition Blank A evaporated at RH=40%. The droplet is tilted by 20°. The green trajectories correspond to particles located to the left of the gravity vector, while the red trajectories correspond to those on the right.

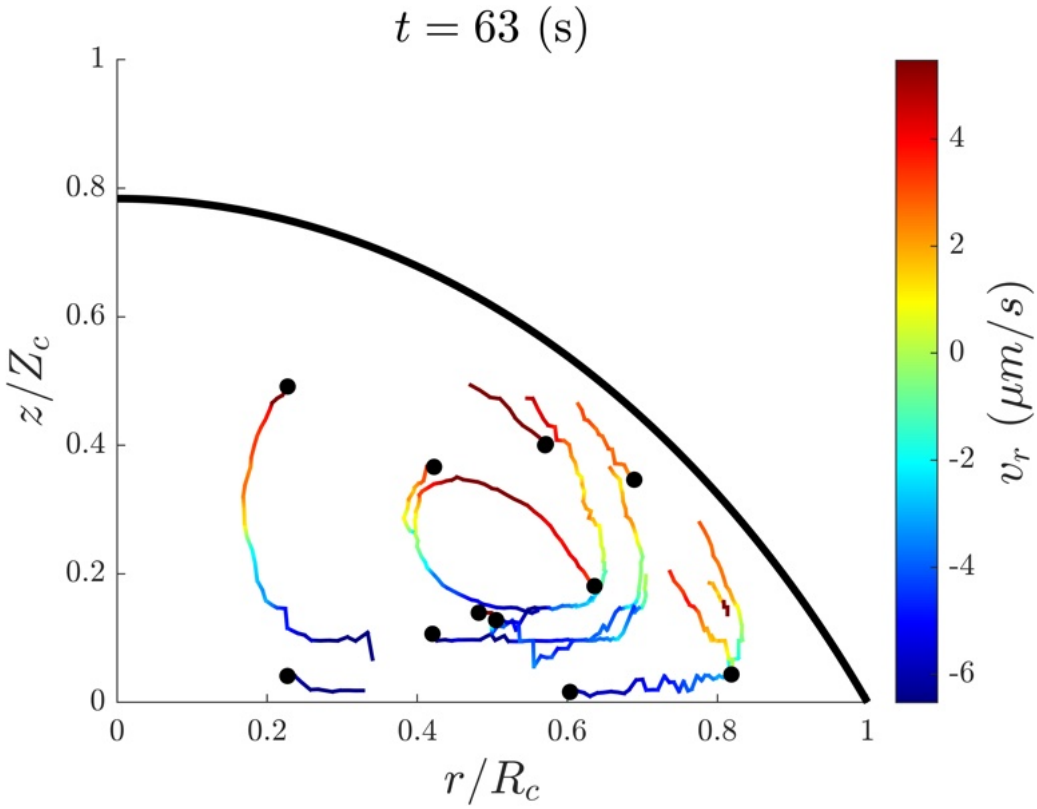

Figure 10: GDPT measurements of particle trajectories obtained during a first stage of the droplet evaporation process. The interface has not receded enough to capture enough particles. Thus, particles remain in the bulk, where they describe the recirculatory motion studied experimentally and theoretically in the main text. Drop of composition Blank A, initial volume 0.5 µL, evaporated at RH=40%.

the contact line is not possible due to the high protein concentration, which makes the region overly dark. However, in the inner regions of the deposit, where the protein content is lower, the observed structures qualitatively resemble those seen in composition A.

Using TEM, we can study shallow dendritic crystals such as the one shown in Fig. 15C, where virions are observed aggregated in the vicinity of the crystals. Recently, by means of fluorescence microscopy other groups have reported co-localization of fluorescent nanoparticles and/or bacteria with

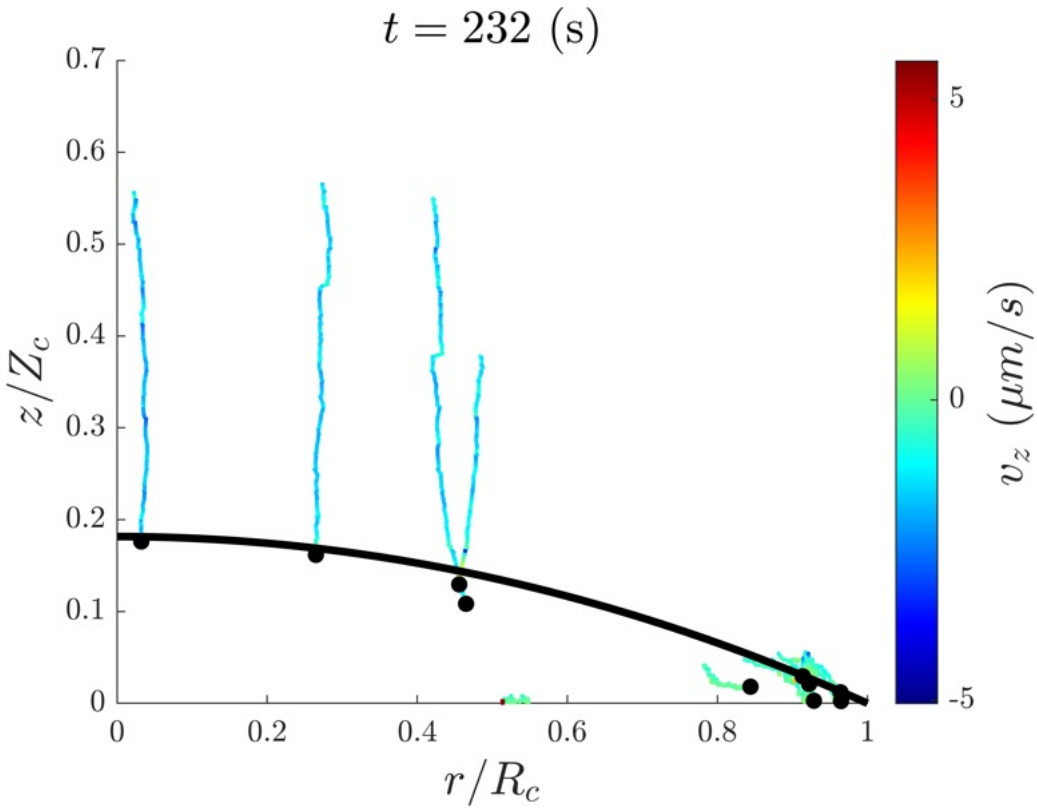

Figure 11: GDPT measurements of particle trajectories obtained during the last stage of the droplet evaporation process. The interface has receded substantially with respect to its initial position, which has lead to the capture of the tracer particles. Drop of composition Blank A, initial volume 0.5 µL, evaporated at RH=40%.

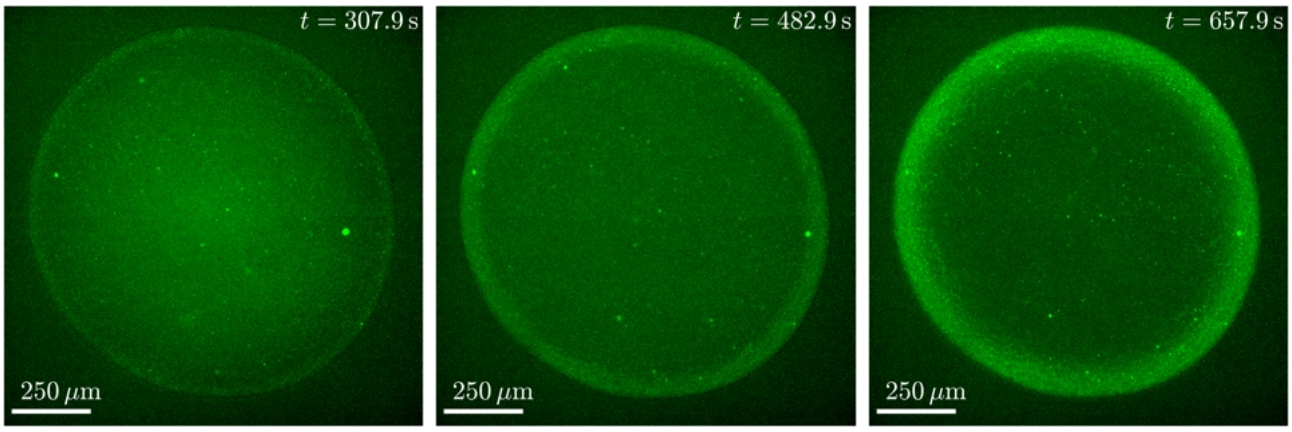

Figure 12: Subsequent fluorescent images of a droplet of composition A evaporating at RH=70%

salt crystals [62, 23, 14, 63]. The reduced spatial resolution of this technique prevents these studies from determining whether virions are actually embedded within the crystals, or merely surrounding them. Fig. 15D displays a globular crystalline structure appears, while in panel F (which shows the same image in high contrast) the crystal appears darker, allowing clearer visualization of the surrounding virion aggregates. Remarkably, virions are trapped in protein regions and surrounding the outermost globular crystals. We cannot directly observe the inside of the general structure, but the aggregates of virions persist until reaching the crystal edge. We observe densely packed virion aggregates trapped at the crystal edge, where everything appears darker. In panel (f), we can observe globular crystals emerging within the region of viral aggregation. Some of these crystals exhibit a

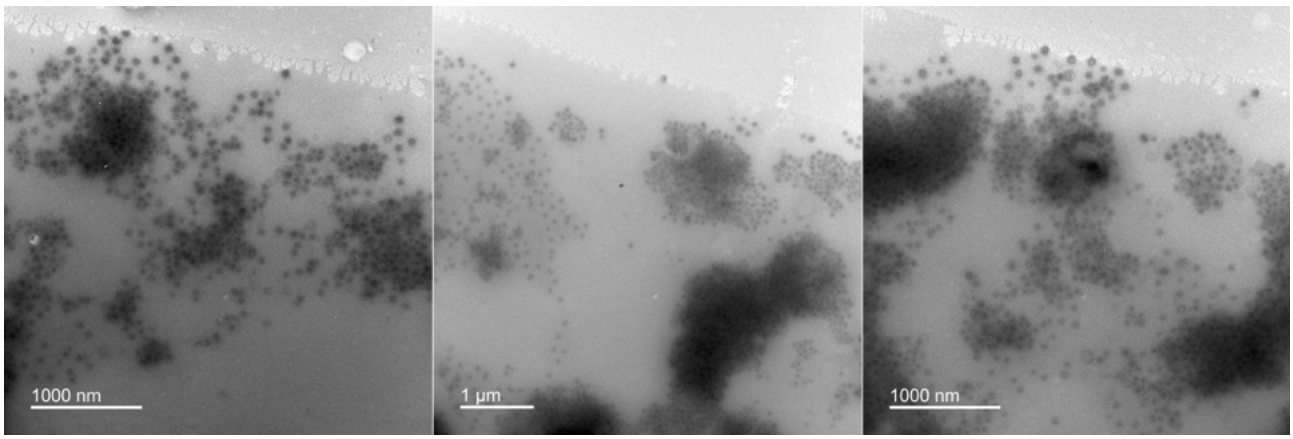

Figure 13: TEM images of the residue of a droplet of composition A evaporated at RH = 40%.

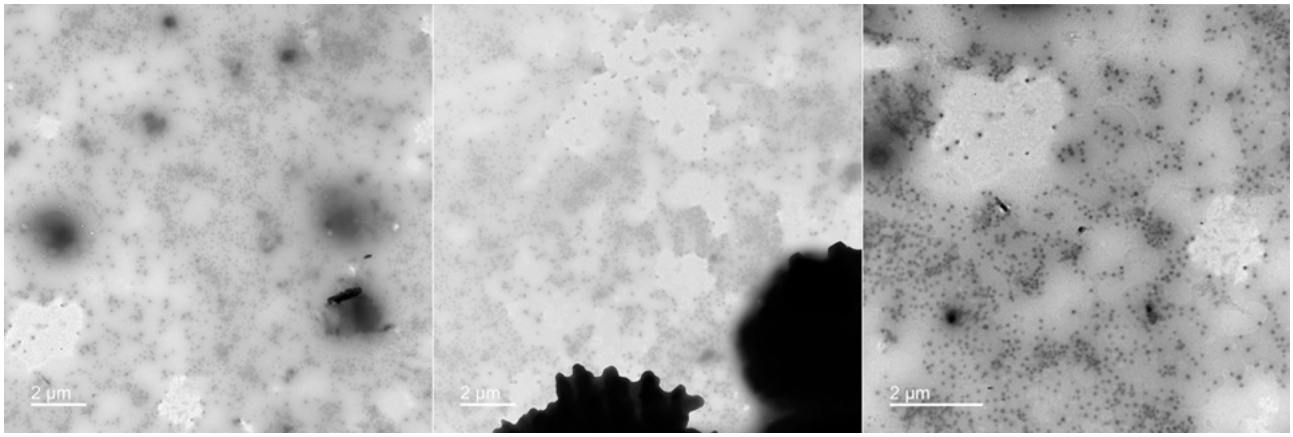

Figure 14: TEM images of the residue of a droplet of composition A evaporated at RH = 40%.

spherical appearance similar to virions but are slightly larger. This phenomenon is consistent for the drops of the two compositions studied here. This leads us to hypothesize that virions may act as nucleation sites for crystals, a phenomenon reported by other researchers in ice nucleation studies. Adams and colleagues [64] studied the freezing of droplets and found that the ϕ6 coronavirus has ice-nucleating activity. This striking phenomenon needs to be further studied. Also, we future studies will confirm the salt/protein proportion in the composition of the crystals shown in Fig. 15, as we cannot rule out at the moment that they are protein, not salt, crystals.

Fig. 16 shows TEM images of the dry residue from a droplet of composition A evaporated at RH=70%. In image (a), the contrast between the contact line region and the inner region is low, indicating a more uniform protein distribution compared to droplets evaporated at RH=40%. Virions also appear more evenly distributed throughout the droplet. Inset (b), taken near the contact line, shows a lower concentration of virions than observed at RH=40% (see Fig. 1 in the main text). Crystallization is still present at RH=70%, with virions observed surrounding the crystals.

Model simulations for different conditions

To verify that the flow pattern is similar for both compositions used on our experiments, and more importantly compared to a droplet that only contains artificial saliva, we carried different simulations of our model. In Fig. 18 we show that the flow pattern of an evaporating droplet of artificial saliva is also recirculatory. Importantly the order of magnitude of the velocity is comparable to compositions blank A and blank B. For completeness, in Fig. 19 we show a snapshot of a simulation of the evaporation of a droplet of composition blank B at RH=40%.

Finally, we include in Fig. 20 a snapshot of a simulation of an evaporating artificial saliva droplet

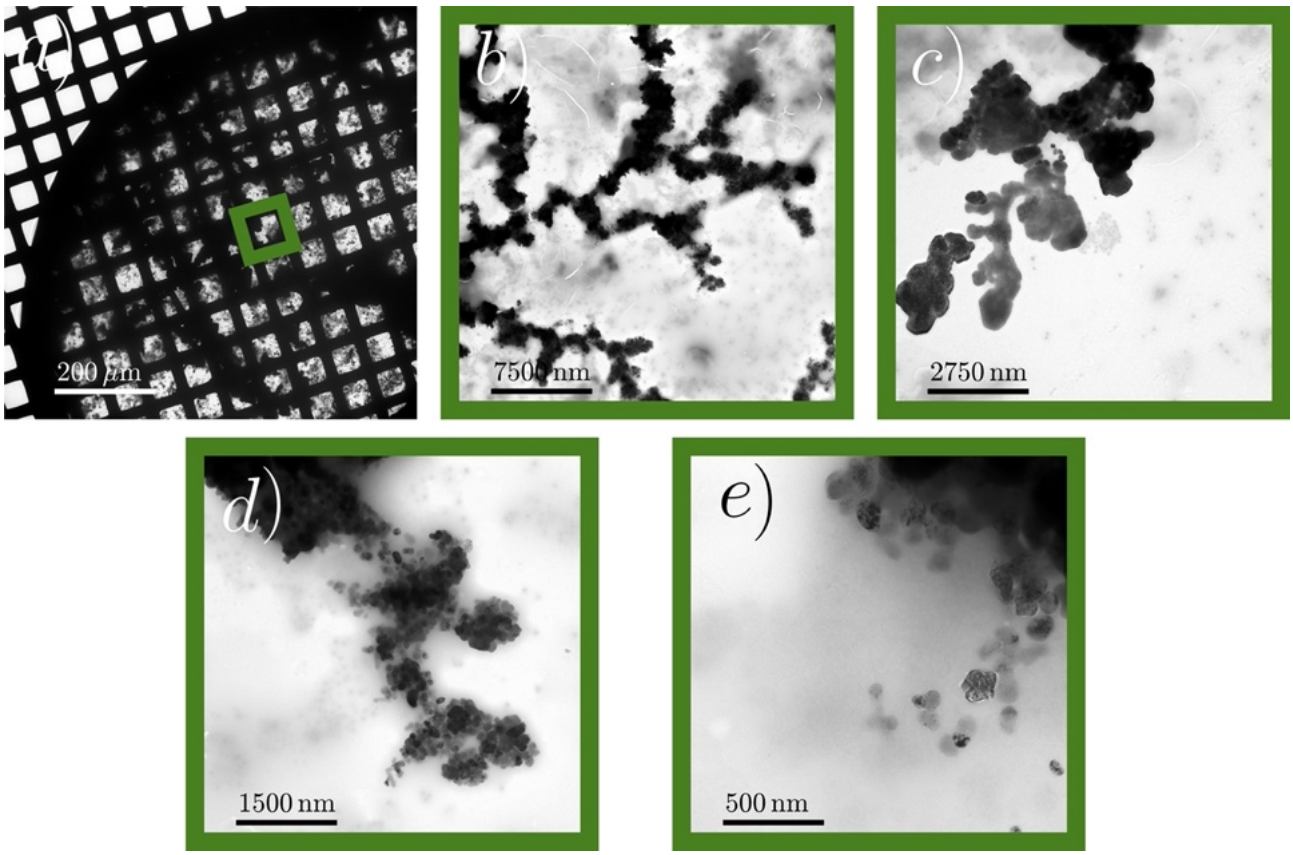

Figure 15: TEM images of the residue of a droplet of composition B evaporated at RH = 40%. (a) Global view of the drop residue on the TEM grid. (b-d) where taken in the inner region of the dry residue. The high content amount of protein at the contact line for this composition does not allow us to visualize that region of the residue.

at RH = 70%. Interestingly, at this relative humidity the evaporation is slower, allowing the solutes more time to diffuse in the vertical direction. As a result, smoother vertical gradients in solute concentration, and consequently in density, are observed. The reduced strength of natural convection accounts for the lower order of magnitude of the velocity field observed at RH = 70%.

Supplementary movies

- Movie S1. Experimental video of PTV on a droplet of composition B, evaporated at Hr=40%.
- Movie S2. Experimental video of the bottom view used to reconstruct the 3D velocity field thanks to the GDPT technique. Notice that the ellipsoidal shape of the contact line is due to the use of a cylindrical lens to sharp how particles defocused for different optical axis positions.
- Movie S3. Trajectories obtained with GDPT from Movie S2. The droplet of composition blank B was evaporated at Hr=40%.
- Movie S4. Video of a simulation corresponding to the experiment shown in Fig. 1 on the main text.
- Movie S5. Video of a fluorescent experiment on a droplet of composition blank B evaporated at Hr=40%.
- Movie S6. Evidence of strong flows directed towards salt crystals while they are growing.

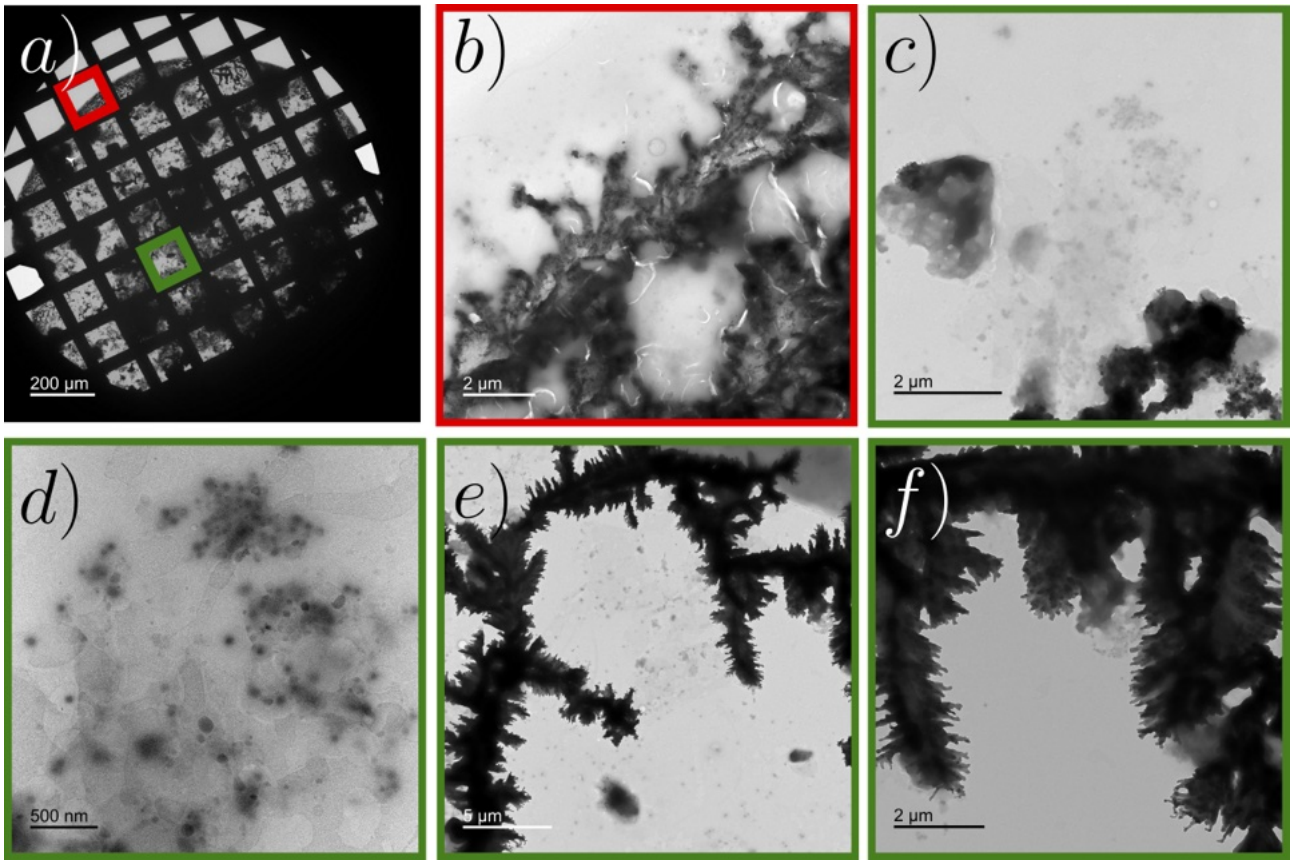

Figure 16: TEM images of the residue of a droplet of composition E evaporated at RH = 70%. The red images is taken at the contact line, whereas the green images where taken in the inner region of the dry residue.

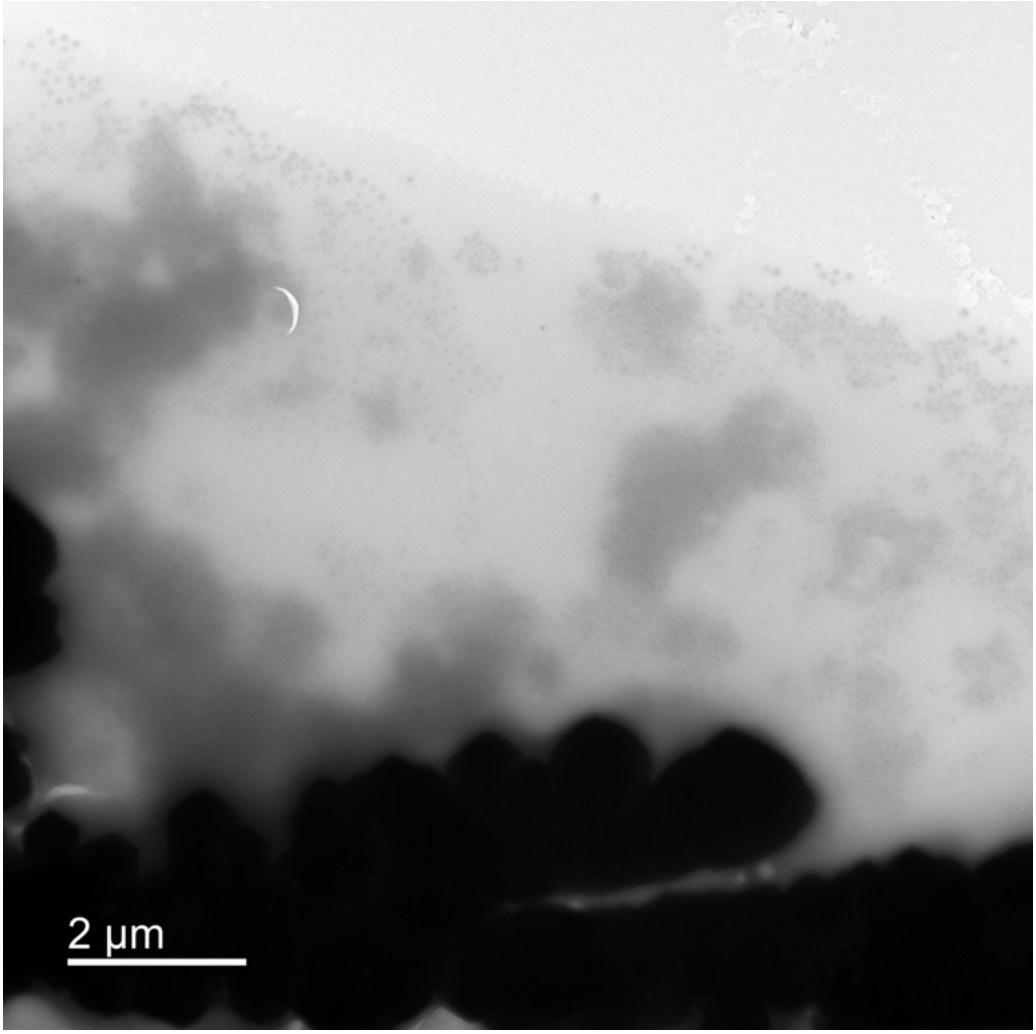

Figure 17: TEM image of a region close to the contact line of a droplet of composition A evaporated at RH = 40%. We see a dendritic salt crystal with neighboring viral aggregates. The image is slightly defocused to be able to see the salt crystal and the virions simultaneously, owing to the fact that the crystal is much taller than the viral aggregates.

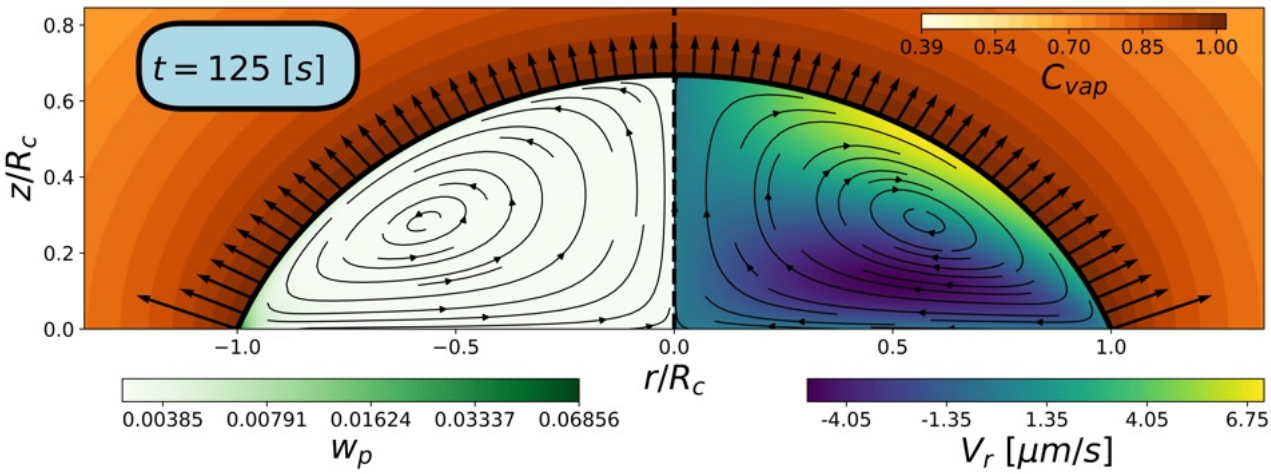

Figure 18: Simulations of a droplet of artificial saliva evaporated at RH=40%.

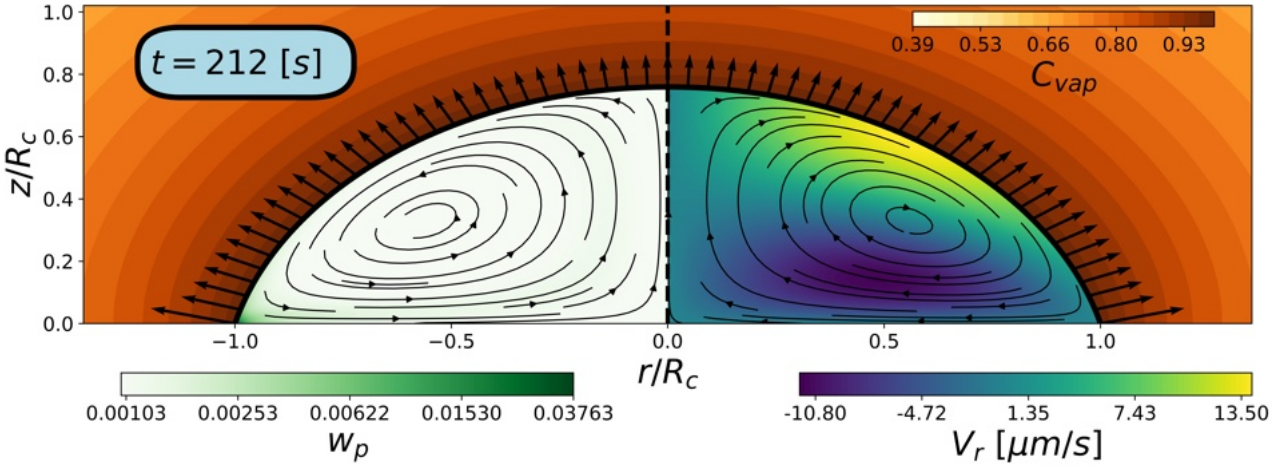

Figure 19: Simulations of a droplet of composition blank B evaporated at RH=40%

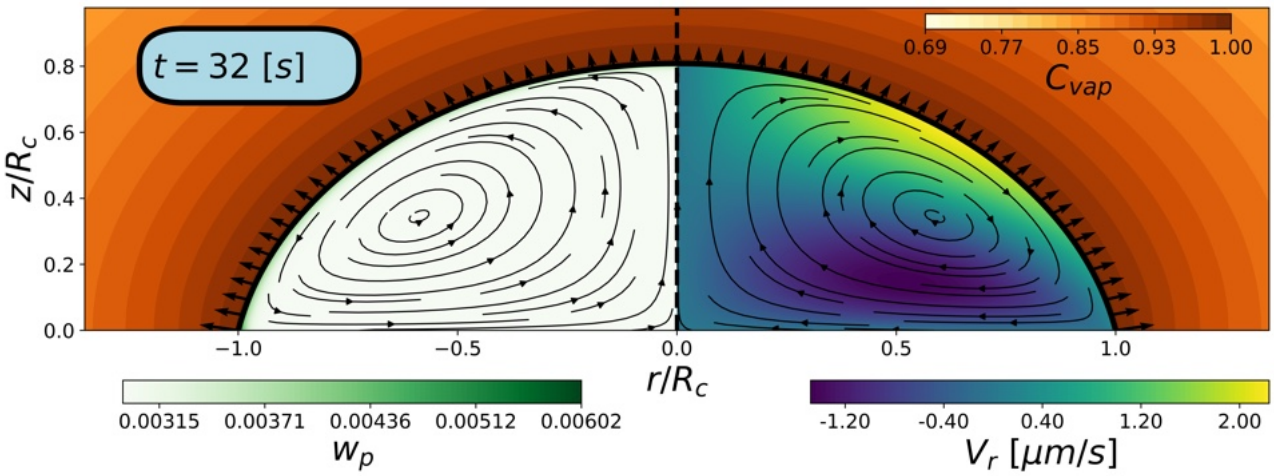

Figure 20: Simulations of a droplet of artificial saliva evaporated at RH=70%.